The Behavior of Rare Earth Elements during Green Clay Authigenesis on the Congo Continental Shelf

Germain Bayon, Pierre Giresse, Hongjin Chen, Marie-Laure Rouget, Bleuenn Gueguen, Gabriel Ribeiro Moizinho, Jean-Alix Barrat, Daniel Beaufort

▶ **To cite this version:**

Germain Bayon, Pierre Giresse, Hongjin Chen, Marie-Laure Rouget, Bleuenn Gueguen, et al.. The Behavior of Rare Earth Elements during Green Clay Authigenesis on the Congo Continental Shelf. Minerals, 2023, 13 (8), 1081 (23p.). 10.3390/min13081081 . hal-04204160

HAL Id: hal-04204160
https://hal.science/hal-04204160

Submitted on 13 Sep 2023

HAL is a multi-disciplinary open access archive for the deposit and dissemination of scientific research documents, whether they are published or not. The documents may come from teaching and research institutions in France or abroad, or from public or private research centers.

L'archive ouverte pluridisciplinaire **HAL**, est destinée au dépôt et à la diffusion de documents scientifiques de niveau recherche, publiés ou non, émanant des établissements d'enseignement et de recherche français ou étrangers, des laboratoires publics ou privés.

Distributed under a Creative Commons Attribution 4.0 International License

minerals

MDPI

Article

The Behavior of Rare Earth Elements during Green Clay Authigenesis on the Congo Continental Shelf

Germain Bayon [1,*], Pierre Giresse [2], Hongjin Chen [1,3], Marie-Laure Rouget [1], Bleuenn Gueguen [1], Gabriel Ribeiro Moizinho [1,4,5], Jean-Alix Barrat [6] and Daniel Beaufort [7]

1 Univ Brest, CNRS, Ifremer, Geo-Ocean, F-29280 Plouzané, France; chenhongjin15@mails.ucas.ac.cn (H.C.); marie-laure.rouget@univ-brest.fr (M.-L.R.); bleuenn.gueguen@univ-brest.fr (B.G.); gabriel.ribeiro.moizinho@ifremer.fr (G.R.M.)
2 Centre of Education and Research on Mediterranean Environments (CEFREM), UMR CNRS 5110, Perpignan Via Domitia University, F-66860 Perpignan, France; giresse@univ-perp.fr
3 Key Laboratory of Marine Mineral Resources, Ministry of Natural Resources, Guangzhou Marine Geological Survey, China Geological Survey, Guangzhou 510760, China
4 Géosciences-Environnement Toulouse, Université de Toulouse, UPS (SVT-OMP), CNRS, IRD, F-31400 Toulouse, France
5 Instituto de Geociências, Universidade de Brasília, Campus Universitário Darcy Ribeiro, Ala Central, Brasília 70910-900, DF, Brazil
6 Univ Brest, CNRS, LEMAR, Institut Universitaire Européen de la Mer (IUEM), F-29280 Plouzané, France; barrat@univ-brest.fr
7 Université de Poitiers, IC2MP-UMR 7285-CNRS, F-86073 Poitiers, France; daniel.beaufort@univ-poitiers.fr
* Correspondence: gbayon@ifremer.fr; Tel.: +33-2-98-22-44-54

Abstract: Clay mineral authigenesis at continental margins plays an important role in global marine element cycles. However, despite being increasingly used as tracers for both modern and past oceanographic conditions, the behavior of the rare earth elements (REEs) and their isotopes during marine clay authigenesis still remains poorly known. In this study, we report on a detailed geochemical investigation of glauconite from the West African continental shelf, near the mouth of the Congo River. Elemental, neodymium, and hafnium isotope analyses were conducted on both acid leachate and separated clay-size fractions of glauconite pellets, in order to investigate the behavior of REE during the formation of authigenic clays. Our data indicate that kaolinite dissolution and subsequent Fe-bearing clay authigenesis act as a net source of REEs to seawater. We show that enhanced glauconitization, as inferred from increasing Fe and K contents, is accompanied by significant decoupling of the REE toward markedly LREE-enriched shale-normalized patterns in neoformed clay separates. Using both Nd and Hf isotopes and SEM observations, we rule out any seawater influence and argue that this shift primarily reflects the progressively overwhelming presence of insoluble nanocrystals of detrital LREE-rich phosphates, which are known to occur in close association with kaolinite in tropical soils. Due to their marked insolubility in surface environments, such nanocrystals can be preserved during kaolinite dissolution and subsequently incorporated into the aggregates of authigenic green clays forming the peloids. Most strikingly, we show that the combined influence of net REE loss (due to kaolinite dissolution) and decoupling (due to subsequent entrapment of inherited LREE-bearing accessory phases into neoformed clay minerals) is accompanied by preferential release of a dissolved REE fraction characterized by seawater-like distribution patterns. These findings reinforce the emerging view that clay mineral dissolution and authigenesis at continental margins possibly play a major role in marine REE cycling.

Keywords: neodymium; hafnium; kaolinite; phosphate minerals; green marine clay authigenesis

check for updates

Citation: Bayon, G.; Giresse, P.; Chen, H.; Rouget, M.-L.; Gueguen, B.; Moizinho, G.R.; Barrat, J.-A.; Beaufort, D. The Behavior of Rare Earth Elements during Green Clay Authigenesis on the Congo Continental Shelf. *Minerals* **2023**, *13*, 1081. https://doi.org/10.3390/min13081081

Academic Editor: Santanu Banerjee

Received: 10 May 2023
Revised: 31 July 2023
Accepted: 9 August 2023
Published: 14 August 2023

Copyright: © 2023 by the authors. Licensee MDPI, Basel, Switzerland. This article is an open access article distributed under the terms and conditions of the Creative Commons Attribution (CC BY) license (https://creativecommons.org/licenses/by/4.0/).

1. Introduction

Authigenic clay mineral formation occurs widely on continental margins, driven by the dissolution of reactive phases such as primary silicate minerals, biogenic silica, and Al- and

Fe-oxyhydroxides [1]. This process is commonly referred to as reverse weathering, because unlike continental silicate weathering, it acts as a major sink for many elements in the ocean, but also as a net source of CO_2 to the atmosphere–ocean system. Reverse weathering takes place in organic-rich sediments deposited in deltaic systems such as the Amazon Fan [1], but fast retrograde clay mineral reactions can also proceed at the deep seafloor [2–5]. Extensive authigenic clay formation may have also prevailed in ancient oceans, especially during the Precambrian, when presumably a much higher dissolved silica concentration in seawater possibly played an important role in the global carbon cycle and Earth's climate [6,7]. While growing evidence exists for the importance of clay mineral authigenesis in the oceanic geochemical cycle of major elements such as Si, K, Mg, and Fe [2–5], the behavior of trace elements during reverse weathering still remains poorly constrained. Understanding the impact of marine clay authigenesis on the cycling of trace elements and their isotopes in the ocean is of particular importance because of their widespread use as paleoceanographic and paleoenvironmental tracers in the sedimentary record. Rare earth elements (REEs) are one the most extensively studied groups of trace elements for reconstructing modern and past oceanographic conditions, particularly via the use of radiogenic neodymium (Nd) isotopes [8,9]. While earlier studies argued that the oceanic REE budget was dominated by riverine inputs and the dissolution of aeolian dusts in surface waters [10], recent work has led to the proposal that REE and Nd isotope budgets in the ocean are strongly influenced by exchange processes taking place at continental margins [11,12], particularly via coupled clay mineral dissolution and authigenesis in marine sediments [13–15]. To date, however, there is still a lack of conceptual understanding of the behavior of REEs during marine clay authigenesis.

In this study, we analyzed a suite of authigenic clays separated from green aluminosilicate pellets formed on the continental shelf near the mouth of the Congo River (Figure 1). Our geochemical investigation includes the measurement of neodymium (Nd) and hafnium (Hf) isotope ratios, in addition to the major and trace element abundances. In the eastern South Atlantic, the distribution of Nd isotopes in the upper water column is relatively homogeneous [16], displaying ε_{Nd} values ~−15.5 (i.e., Nd isotopic ratios expressed relative to the chondritic uniform reservoir) that largely reflect the contribution of riverine inputs from the Congo River combined with intense particulate–seawater exchange processes in the water column, which collectively strongly influence regional marine elemental budgets [16–18]. In contrast to Nd isotopes, which are not significantly decoupled during Earth surface processes and thus serve as powerful proxies for provenance in the sedimentary record [19,20], radiogenic Hf isotopes can be significantly impacted by the dissolution of terrigenous material in both continental and marine environments [21–23]. In most rocks, soils, and suspended sediments, the Hf budget is dominated by zircon; a highly resistant accessory mineral characterized by low lutetium–hafnium (Lu/Hf) and low (unradiogenic) ε_{Hf} compositions compared to other rock-forming minerals [24,25]. Additionally, continental chemical weathering typically leads to the preferential dissolution of accessory phosphate minerals (e.g., apatite) and other Lu-rich mineral phases such as allanite and sphene [21,26], which release a fraction of radiogenic Hf (with high ε_{Hf} values) to nearby surface environments. The combination of these two processes (i.e., 'zircon' effect and preferential dissolution of Lu-rich minerals) explains why river waters and seawater are typically characterized by more radiogenic Hf isotope compositions compared to regional detrital sources [16,21–23,27,28]. The decoupling between Nd and Hf isotopes during Earth surface processes is best illustrated in a ε_{Nd} vs. ε_{Hf} diagram (Figure 2a), where river waters and seawater define a global 'seawater array' [29] that lies well above the 'terrestrial array' defined by most igneous rocks and bulk sediments [30,31]. On continents, the same processes also explain why detrital clays formed in soils during chemical weathering typically display more radiogenic Hf isotope compositions compared to the corresponding coarse-grained, zircon-rich, sediment fractions dominated by primary minerals [32–35]. In the ε_{Nd} vs. ε_{Hf} plot, the clay-size fraction of detrital sediments define a global 'clay array' [35] that distinctively lies between the 'seawater array' and the 'terrestrial array' (Figure 2a). All of

the above characteristics make the combined use of Hf–Nd isotopes in clay-size sediments particularly well-suited for investigating continental chemical weathering processes in the sedimentary record [36–38]. Similarly, the application of Hf–Nd isotopes to marine authigenic clays is expected to provide unique constraints on the behavior of trace elements during reverse weathering, particularly for REEs.

2. Green Clay Authigenesis at the Congo Shelf

The Congolese Shelf is a relatively flat 40-to-80 km wide platform that extends from coastal West Africa to the continental shelf-break located at about a 120 m water depth (Figure 1). Regional oceanography at the Congo Shelf is dominated by the northward flowing Benguela Coastal Current (BCC) and the Congo freshwater discharge (i.e., the second largest river on Earth by discharge volume) (Figure 1). In its pathway, the BCC entrains the Congo River plume northward along the coast of Cabinda and Congo while substantial sediment loads exported by the Congo River are channeled into the Congo submarine canyon, whose head directly lies within the river estuary [39], a large fraction of suspended particulates is transported northward within the Congo plume and subsequently deposited at the Congolese Shelf (Figure 1). About 180 km away from the mouth of the Congo River, the resulting mud deposit composed of abundant fecal pellets extends up to 45-km offshore of Pointe-Noire [40] (Figure 1). At this location, the deposition of Congo River-borne particulates associated with substantial amounts of kaolinite, reactive iron minerals, and terrestrial organic carbon drives intense marine clay authigenesis, resulting in the extensive formation of glauconitic grains [40,41]. The exceptionally high contents of sedimentary iron in the muds of this area (up to 20%–30% Fe_2O_3) constitute one of the determining conditions for glauconitization at the Congo margin [41].

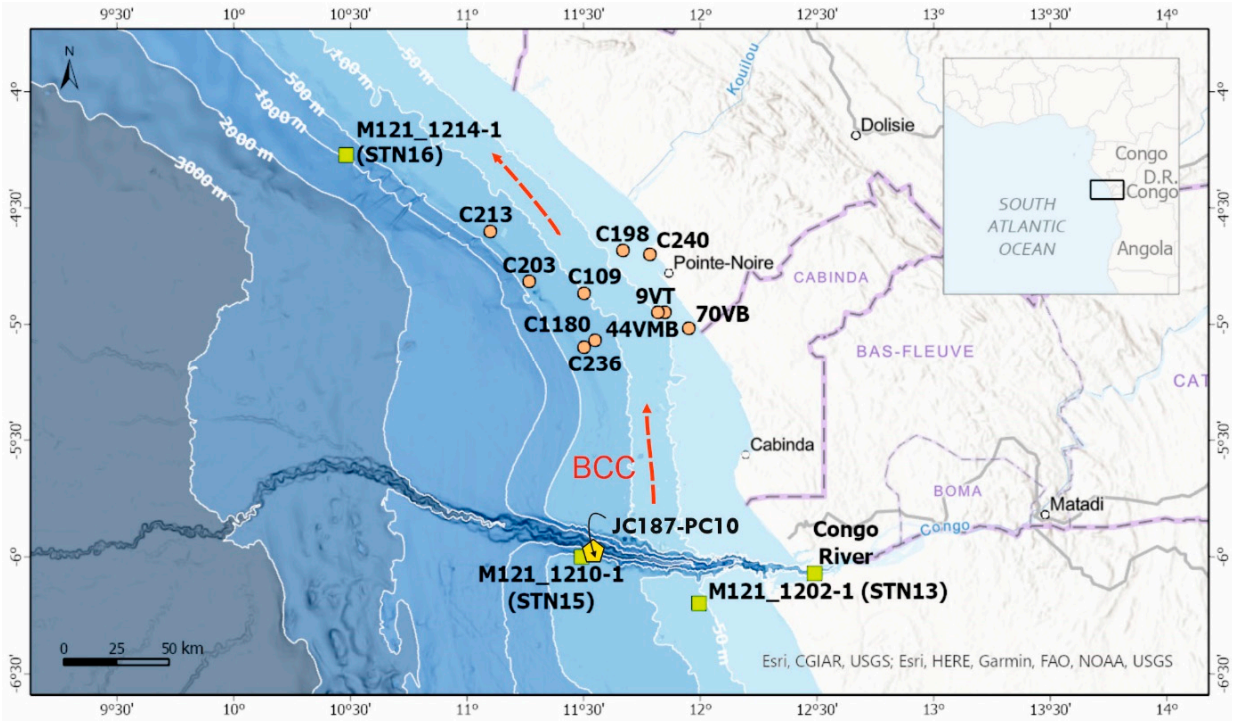

Figure 1. Bathymetric map of the West African margin and location of the studied samples. The red dotted arrows represent the flow trajectory of the Benguela Coastal Current (BCC), which redistributes kaolinite-rich Congo River-borne suspended material northward along the Congo Shelf. Orange circles indicate the location of sediment cores containing glauconite pellets analyzed

in this study, all recovered from the large mud deposit fed by fine-grained sediment fluxes from the Congo River. Note that the distribution maps of both the mud deposit and glauconitic grains in the study area are reported in [40]. All samples were collected from surficial sediment samples (0–10 cm core depth), except for core C213. The location and name of hydrographic stations (green squares) used for comparative Nd–Hf isotope data for seawater and river water [16] are also shown, as for the sediment core (JC187-PC10) used for characterizing the average major and trace element composition of the clay-size detrital fraction exported by the Congo River.

On the West African continental shelf, fecal pellets represent the main substrate for green clay authigenesis and glauconitization [41,42]. Under relatively high sedimentation rates, the formation of authigenic Fe-bearing phyllosilicates proceeds from the transformation of kaolinite into 7 Å Fe-rich phases, which involves the substitution of Fe and Mg for Al in octahedral sheets [41]. This process involves successive steps of dissolution–recrystallization reactions, which take place over a timescale of ~10^2–10^3 years [43]. During this process, progressive Al loss resulting from kaolinite transformation leads to goethite neoformation.

When fecal pellets remain for a longer period of time at the sediment–water interface under low sedimentation rate conditions, kaolinite dissolution and the subsequent neoformation of micaceous layers also involves the fixation of K from seawater. After the complete disappearance of kaolinite, green clay neoformation evolves from a smectite-like composition, with K_2O contents of 2%–3%, toward a more evolved glauconitic composition with K_2O up to 5%–6%. This process is typically achieved over 10^4 year timescales, and is generally not accompanied by any further increase in Fe_2O_3 content [44]. The neoformation of K-rich mica-like silicates may occur either at the expense of the 7 Å Fe-bearing authigenic phase, or directly from recrystallization following kaolinite dissolution. At the Congo Shelf, an empirical relationship is observed between the composition of glauconitic pellets and water depth, which relates to their age of formation, with older pellets being encountered at deeper shelf settings characterized by slower sedimentation rates [41].

The mineralogical composition of peloid populations on the Congo Shelf has been thoroughly investigated in previous studies through XRD analyses of different density fractions of green grains [41,45]. Representative X-ray diffractograms are presented for selected pellets from the same study area (Figure 3). The samples collected in coastal environments subject to relatively high sedimentation rates are dominated by immature green peloids containing 7 Å Fe-rich clay mineral phases (Figure 3a). Measurements of d_{060} for those 7 Å minerals in various density fractions indicate the progressive transformation of kaolinite into trioctahedral l:1 phyllosilicates in these pellets. Projection of the chemical composition inferred from the approximate crystallochemical formula onto a classification field confirmed the transformation of kaolinite into a 7 Å Fe-rich phase via the substitution of Fe^{2+} and Mg for Al in the octahedral sheet, with negligible changes in the tetrahedral sheet [41,45]. The resulting intermediate phase has a composition closer to greenalite than berthierine, suggesting that the evolution process may have been inhibited by the formation of goethite [41,45]. In contrast, XRD measurements conducted on density-specific fractions of samples from more distal outer shelf environments indicate that the heaviest fractions in these samples, dominated by shiny and finely cracked ovoidal peloids, are mostly composed of goethite (Figure 3b). The X-ray diffractograms corresponding to lighter density fractions indicate the ongoing neoformation of a 10 Å mineral phase corresponding to glauconite. The 10 Å authigenic minerals formed in mature grains from the outer shelf display a relatively homogenous composition and typically occur in close association with goethite and quartz [41,45].

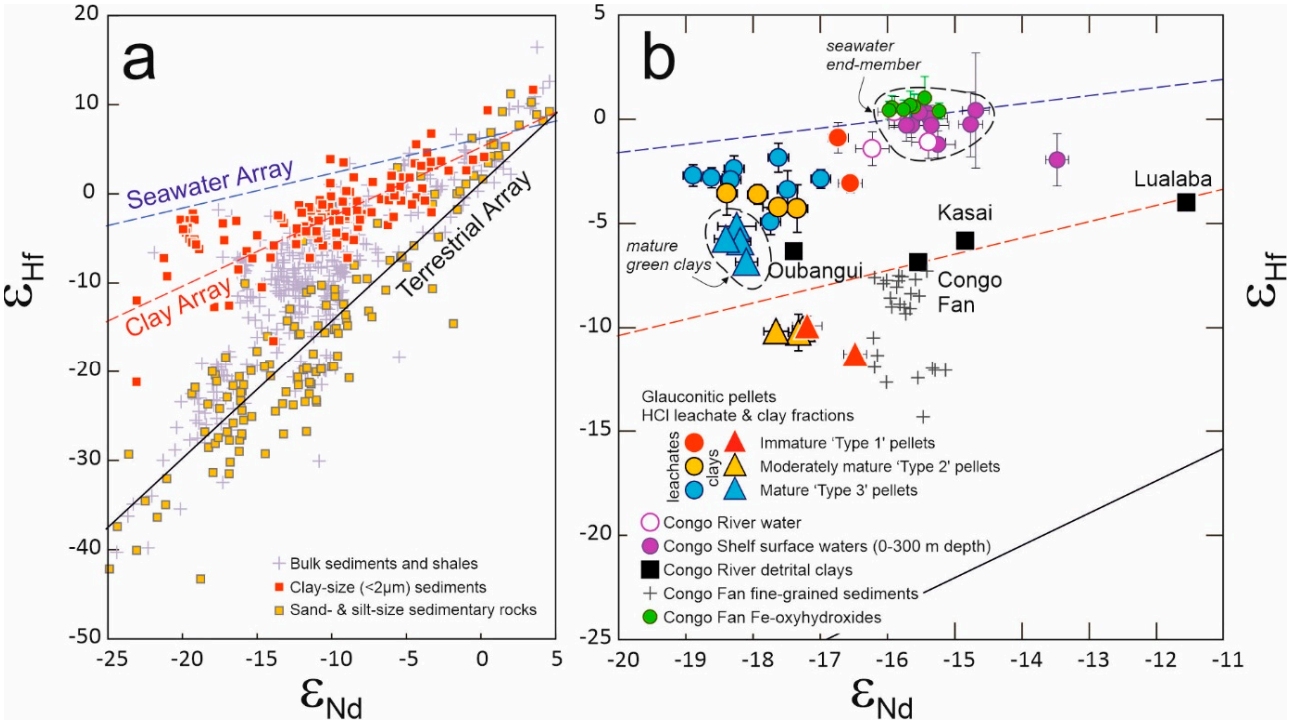

Figure 2. Neodymium and hafnium isotopes in the sedimentary system. (**a**) Nd–Hf isotope compositions of bulk modern marine sediments, ancient shales and sandstones, and clay- and silt-size fractions of modern river sediments [30,31,35]. The terrestrial array corresponds to the correlation defined by all terrestrial rocks including bulk sedimentary rocks [30,31], while the clay array ($\varepsilon_{Hf} = 0.78 \times \varepsilon_{Nd} + 5.23$) refers to the linear regression based on fluvial clays and the clay-size fractions of modern sediments [35]. The seawater array includes the Nd–Hf isotope data for seawater and marine ferromanganese crusts and nodules [29]. (**b**) Nd–Hf isotope data for the acid leachate and separated clay-size fractions of studied glauconite grains from the Congo Shelf. Data for Congo River and upper surface waters (<300 m water depth) at the Congo Shelf are from [16]. 'Type 1′ samples correspond to immature multi-pellet samples containing Fe-bearing green clays, while 'Type 2′ samples are dominated by authigenic 7 Å Fe-rich mineral phases. The 'Type 3′ samples correspond to mature glauconite-bearing samples. Additionally shown for comparison are the Hf–Nd isotope data for leached sedimentary Fe-oxyhydroxides [32] and fine-grained sediments from the Congo Fan [35,46], and clay-size fractions of suspended particulates from the Oubangui, Kasai, and Lualaba (i.e., the main tributaries of the Congo River) [36,47].

A former pioneering study already reported elemental and Nd–Sr isotope data for glauconite formed at the Congo Shelf [49]. After identifying the presence of several detrital and seawater-derived components within the pellets, the authors concluded that glauconite formation was accompanied by progressive incorporation of an authigenic phosphate-rich phase, arguing that mature grains with $K_2O > 6.5\%$ displayed seawater Nd isotope compositions [49]. In this new study, we revise this interpretation, taking advantage of the fact that both water masses and detrital sediment sources at the Congo Shelf are now fully characterized for Nd and Hf isotopes.

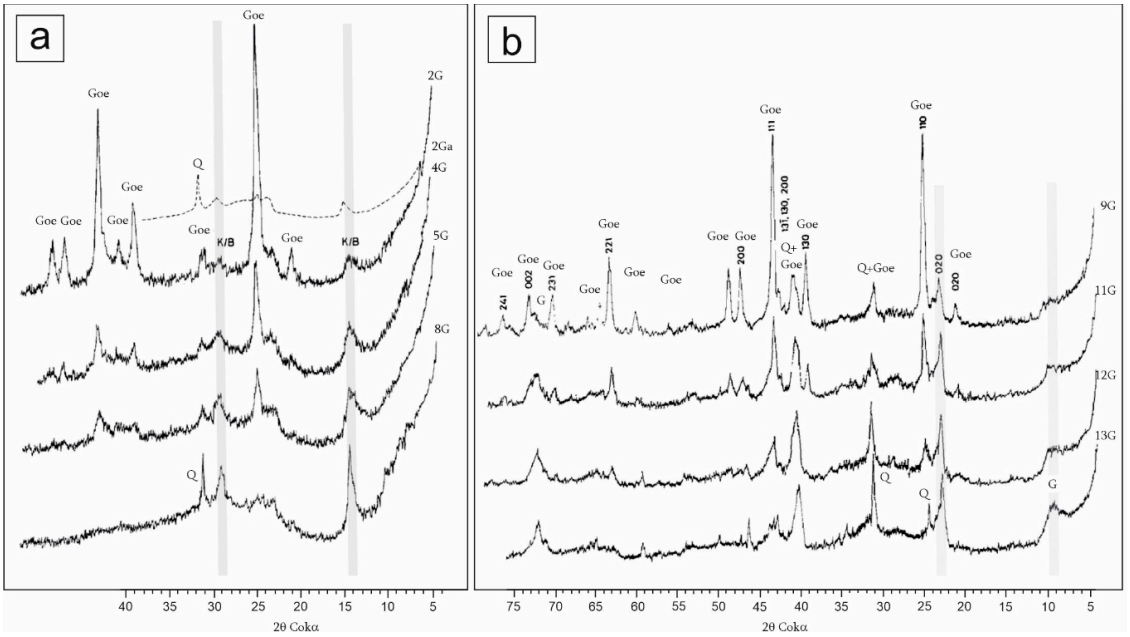

Figure 3. X-ray diffraction patterns of different density fractions from green pellets of the Congo Shelf (adapted from [41,45]). (**a**) 'Type 1' sample 191 (coastal region; near core 70 VB). 2Ga (dashed line) is sample 2G treated with HCl to remove iron oxides. Goe: goethite; K: kaolinite; B: 7°θ Cokα Fe-rich phase; Q: quartz. The grey bands around 14 and around 29°θ Cokα indicate the progress of the neoformation of iron-rich green clay minerals (7 Å phase). (**b**) 'Type 3' sample 210 (outer shelf region; near core 213). 9G: d > 2.78; 11G: 2.70 < d < 2-78; 12G: 2.64 < d < 2.70; 13G: 2.53 < d < 2.64. Goe: goethite; G: glauconite; Q: quartz. The grey bands around 9°θ Cokα (001) and around 23°θ Cokα (020) indicate the progress of glauconite neoformation (adapted from [41,45,48]).

3. Materials and Methods

3.1. Studied Glauconitic Pellets

Selected glauconitic grains for this study were recovered at the continental shelf about ~75 to 180 km northward of the mouth of the Congo River (Figure 1). The inner (shallower) part of the plateau is directly under the influence of the BCC and is characterized by relatively high sedimentation rates. The outer continental shelf exhibits reduced sedimentation rates, and is the location of one of the most productive "glauconite factories" in the Gulf of Guinea [40,42]. Ten surface sediment samples collected between a 16 and 200 m water depth were analyzed in this study, corresponding to representative successive stages of green clay authigenesis (Table 1). As above-mentioned, the different stages of glauconitization at the Congolese margin are generally related to the age of corresponding sediment deposits, inferred from the direct radiocarbon dating of large benthic foraminifera (e.g., Amphistegina gibbosa) associated with shelly glauconitic sands or from bulk organic ^{14}C measurements of fine-grained sediments conducted in the context of earlier paleoenvironmental investigations [44,50–52]. All of the studied samples were derived from upper surface sediments (0–10 cm depth below the seafloor, b.s.f.), except for core C213 (113 m water depth), from which five samples were collected from different sediment depths down to 198 cm b.s.f. The surface samples were selected because they correspond to representative sedimentary facies at the Congo Shelf. The different samples recovered in core C213 were chosen because green pellets along this core display a range of facies and elemental compositions indicative of various stages of green clay authigenesis. The inferred ages of the studied green pellets and associated sediment deposits include muds from the last glacial maximum (~20 kyr B.P.), shelly sands from the beginning of the last transgression (~13–12 kyr B.P.), and muds from the active transgression period (~11–6 yr B.P.) and the Holocene sea-level highstand (<6 kyr B.P.) (Table 1).

Table 1. The studied glauconitic sediment samples on the Congo Shelf and estimated age.

#	Sample	Lat S (°)	Long E (°)	Core Depth (cm b.s.f.)	Water Depth (m b.s.l.)	Approx. Age (kyr)	Degree of Glauconitization [a]
1	C240	4°42	11°47	0–10	16	1–2	Type 1
2	70VB	5°01	11°57	0–10	25	2–3	Type 1
3	9VT	4°57	11°51	0–10	41	2–3	Type 2
4	44VMB	4°57	11°49	0–10	46	2–3	Type 2
5	C198	4°41	11°40	0–10	50	4–6	Type 2
6	C109	4°52	11°30	0–10	104	10	Type 2
7	C1180	5°04	11°33	0–10	110	12	Type 3
8	C203	4°49	11°16	0–10	125	20	Type 3
9	C236	5°06	11°30	0–10	200	20	Type 2
10	C213-10	4°36	11°06	10–20	113	10	Type 3
11	C213-39	‘	‘	39–40	‘	12	Type 3
12	C213-90	‘	‘	90–100	‘	13	Type 3
13	C213-130	‘	‘	130–140	‘	15	Type 3
14	C213-198	‘	‘	198	‘	20	Type 1

[a] ‘Type 1’: immature pellets containing Fe-bearing green clays. ‘Type 2’: moderately mature pellets dominated by Fe-bearing green clays. ‘Type 3’: mature pellets dominated by glauconite. b.s.l.—below sea level.

As discussed below, the studied samples were classified into three categories based on the corresponding K_2O and Fe_2O_3 abundances in the separated clay fractions: ‘Type 1′ samples (70VB; C213-198), which correspond to immature multi-pellet samples with relatively low K_2O (between ~1.4 and 2.2%) and Fe_2O_3 (<20%) contents; ‘Type 2′ samples (9VT, 44VMB, C109) with clays exhibiting moderate K_2O (<2.4%) but higher Fe_2O_3 contents (from 20% to 25%), indicative of higher proportions of authigenic 7 Å Fe-rich mineral phases; ‘Type 3′ samples (C203, C213-36, C213-90, C213-130) corresponding to more mature glauconite-bearing samples with clays exhibiting higher K_2O (>3%) and Fe_2O_3 (>25%) contents.

In this study, most green grains formed from fecal pellets produced by mud-eater worms, except for a few samples recovered from a band of relict shelly sediments at about a −100 m water depth (i.e.,18 kyr B.P.), which also included inner molds of organisms such as foraminifera or various fragments of mollusks, sea urchin tests, or bryozoans. This observation indicates that glauconitization can occur in different depositional settings at the Congo Shelf [40,50]. Above a 50 m water depth, glauconitic pellets are mostly grey-green and display an earthy appearance. Shallow grains are also relatively smooth and small (250 to 400 µm in diameter). In contrast, grains from the deeper shelf setting are commonly cracked, dark-green in color, and may reach ~1 mm in diameter. Beyond a 120 m water depth, all glauconitic grains at the Congo Shelf correspond to almost pure green sands, in an environment characterized by low sedimentation rates [41,42,53].

Finally, for comparison purposes, we used the average geochemical composition of detrital clay-size fractions (n = 144) separated from a sediment core (JC187-PC10) recovered from a terrace of the Congo submarine canyon (−5.910° S; 11.332° E; 1666 m water depth; 15.15 m long; Figure 2). These samples were processed using the same chemical and analytical procedures as for the studied green grains. Note that the clay mineral assemblages exported from the Congo River during the late Quaternary have been dominated by kaolinite (between ~45% and 70%), smectite (~15%–40%), illite (~10%–20%), and minor amounts of chlorite (<8%) [54]. The clay-size fraction of marine muds on the Congo Shelf may also contain substantial amounts of quartz (up to ~40%; [41]).

3.2. Sample and Chemical Preparation

The Fe-bearing peloids analyzed in this study were isolated using a paramagnetic separator and then divided by means of density separation using bromoform and methyl alcohol. All samples were thoroughly rinsed in ultrapure water to remove any surficial clays attached to glauconitic pellets, oven dried, and very gently ground in an agate mortar.

The resulting powders were split into two sub-samples for separate analyses on: (1) the acid-leachable fraction of glauconitic pellets, which most likely includes goethite and other Fe-oxyhydroxide phases, biogenic material, and presumably a fraction of neoformed authigenic clays; (2) the separated clay-size fraction of glauconitic pellets composed of both authigenic and detrital clay minerals. For analysis of the acid-leachable fractions, about 50 mg of powder was treated with ultrapure 5 M HCl (80 °C/2 days). For analysis of the clay-size fractions, between 250 and 1000 mg of the sample was treated with a sequential leaching procedure that selectively targets the removal of biogenic carbonate (5% v/v acetic acid; AA), Fe-oxyhydroxide phases (15% v/v AA + 0.5 M hydroxylamine hydrochloride), and organic matter (10% H_20_2). A final leaching step with EDTA was applied to the remaining residue in order to remove any adsorbed elements during previous leaching steps [36]. Note that none of these leachates were analyzed in this study. Finally, clay-size (<2 µm) fractions were separated from the resulting residues by low-speed centrifugation [20]. After drying, between ~25 and 50 mg of ground clay powder was digested in ultrapure concentrated HF–HCl–HNO_3 (140 °C/5 days), followed by evaporation and a final digestion step with ultrapure 6 M HCl (140 °C/2 days). Four samples (C240, C198, C109, C1180) yielded limited amounts of separated clay material (<30 mg) and hence were only analyzed for their 5 M HCl leachates.

3.3. SEM Observations

Tens of green pellets from one 'Type 3' sample (C213-130) were selected for detailed examination by scanning electron microscope (SEM) at the IC2MP Laboratory (Univ. Poitiers) on a JEOL JSM IT500 equipped with secondary electron (SE) and backscatter electron (BSE) detectors coupled with a Bruker Linxeye energy dispersive X-ray spectrometer (EDX). Analytical conditions were as follows: 15 kV, 1 nA, WD 11 mm, 50 s of acquisition time. Prior to analysis, the studied pellets were mounted in epoxy resin (30 mm diameter), diamond polished, and coated with carbon. Specific areas containing accessory mineral phases were selected for high-resolution BSE imaging (15 nm pixel resolution) and chemical mapping by EDS.

3.4. Major and Trace Element Analyses

Major and trace element abundances were determined at the Pôle Spectrométrie Océan (Brest, France) with a Thermo Scientific Element XR sector field (SF) ICP-MS. Elemental abundances were calculated using the Tm addition method following procedures described in [55,56]. Briefly, elemental concentrations in any natural sample can be obtained using the mass of sample (M), the amount of Tm added prior to sample digestion (MTm), and CX, CEr, and CYb, the raw concentrations for X, Er, and Yb in the sample solution, respectively, after correction from the analytical drift, procedural blank, and interferences. Elemental (X) abundances are then calculated using the following equation: $[X] = (MTm \times CX)/((M \times (CTm - CTm^*))$; where CTm* corresponds to the Tm concentration in the sample solution with no spike contribution, calculated using chondritic abundances for Tm, Er, and Yb [56]. The precision and accuracy of the measured abundances were assessed by analyzing a series of certified reference materials including both silicate rocks (AGV-1, BCR-1, AN-G, DNC-1) and ferromanganese deposits (NOD-A1, NOD-P1, GSPN-2, GSPN-3). The precision of measurements given as relative standard deviation (RSD; n = 3) was generally <5% for all elements. Results obtained for reference materials generally agreed <5% for REEs, Zr, Hf, Y, Ba, and TiO_2; <10% for Sr, Th, U, V, Cr, NaO, MgO, Al_2O_3, CaO, and Fe_2O_3; <20% for Li, Rb, P_2O_5, Co, Cu, Mo, and K_2O. In this study, shale-normalized REE abundances were determined using the set of values for World River Average Silt (WRAS; [20]).

3.5. Nd and Hf Isotopic Analyses

Neodymium and hafnium were purified by ion exchange chromatography [46,57] and isotopic measurements were performed with a Thermo Scientific Neptune multi-collector ICP-MS at the Pôle Spectrométrie Océan (Brest, France). Nd and Hf isotopic compositions were determined using a sample-standard bracketing approach with solutions of Nd-SPEX and AMES-Grenoble, respectively, after correction from isobaric interferences. Mass-bias corrections were made using the exponential law using $^{146}Nd/^{144}Nd = 0.7219$ and $^{179}Hf/^{177}Hf = 0.7325$. Repeated analyses of JNdi-1 and JMC-475 standard solutions gave $^{143}Nd/^{144}Nd$ of 0.512114 ± 0.000007 (2σ, n = 6) and $^{176}Hf/^{177}Hf$ of 0.282168 ± 0.000009 (2σ, n = 8), in full agreement with the recommended values of 0.512115 [58] and 0.282163 [59]. Associated uncertainties in the JNdi-1 and JMC-475 analyses correspond to external reproducibilities of ±0.15 ε and ±0.31 ε (2σ), respectively. Note that in-run uncertainties on the measured Hf isotopic ratios were commonly higher (up to ±1.14 ε; 2σ) due to relatively low Hf abundances in the studied acid leachate and clay-size fractions (Table 2). Epsilon values were calculated using present-day chondritic (CHUR) values for $^{143}Nd/^{144}Nd$ (0.512630) and $^{176}Hf/^{177}Hf$ (0.282785) from [60]. The degree of Hf–Nd isotope decoupling in studied clay-size fractions—$\Delta\varepsilon_{Hf\ CLAY}$—was determined using the vertical ε_{Hf} deviation from the 'clay array' using the following equation ($\varepsilon_{Hf} = 0.78 \times \varepsilon_{Nd} + 5.23$; [35]).

Table 2. Nd–Hf isotope compositions of the leached (5 M HCl) and clay-size (<2 µm) fractions of Congo Shelf glauconies.

#	Sample	Degree of Glauconitization [a]	$^{143}Nd/^{144}Nd$		2 se	ε_{Nd}		2 se	$^{176}Hf/^{177}Hf$		2 se	ε_{Hf}		2 se	$De_{Hf\ clay}$
	5 M HCl leachates														
1	C240	Type 1	0.511771	±	0.000008	−16.75	±	0.16	0.282760	±	0.000021	−0.89	±	0.73	6.9
2	70VB	Type 1	0.511782	±	0.000011	−16.55	±	0.22	0.282698	±	0.000013	−3.08	±	0.46	4.6
3	9VT	Type 2	0.511738	±	0.000009	−17.40	±	0.17	0.282664	±	0.000032	−4.28	±	1.14	4.0
4	44VMB	Type 2	0.511746	±	0.000011	−17.25	±	0.22	0.282704	±	0.000013	−2.86	±	0.45	5.2
5	C198	Type 2	0.511687	±	0.000005	−18.39	±	0.10	0.282684	±	0.000029	−3.56	±	1.04	5.6
6	C109	Type 2	0.511720	±	0.000004	−17.74	±	0.08	0.282646	±	0.000018	−4.92	±	0.62	3.7
7	C1180	Type 3	0.511733	±	0.000004	−17.49	±	0.08	0.282690	±	0.000025	−3.37	±	0.90	5.0
8	C203	Type 3	0.511726	±	0.000006	−17.63	±	0.11	0.282733	±	0.000020	−1.84	±	0.70	6.7
9	C236	Type 2	0.511726	±	0.000012	−17.63	±	0.23	0.282665	±	0.000011	−4.23	±	0.41	4.3
10	C213-10	Type 3	0.511661	±	0.000005	−18.89	±	0.09	0.282709	±	0.000015	−2.70	±	0.51	6.8
11	C213-39	Type 3	0.511693	±	0.000004	−18.29	±	0.08	0.282718	±	0.000018	−2.37	±	0.62	6.7
12	C213-90	Type 3	0.511690	±	0.000005	−18.33	±	0.09	0.282703	±	0.000015	−2.91	±	0.54	6.2
13	C213-130	Type 3	0.511676	±	0.000008	−18.62	±	0.16	0.282706	±	0.000014	−2.80	±	0.48	6.5
14	C213-198	Type 1	0.511711	±	0.000005	−17.93	±	0.09	0.282683	±	0.000013	−3.62	±	0.47	5.1
	Clay-size fractions														
2	70VB	Type 1	0.511785	±	0.000009	−16.48	±	0.17	0.282466	±	0.000008	−11.27	±	0.29	−3.6
3	9VT	Type 2	0.511725	±	0.000009	−17.66	±	0.18	0.282497	±	0.000006	−10.17	±	0.22	−1.6
4	44VMB	Type 2	0.511745	±	0.000007	−17.27	±	0.13	0.282501	±	0.000007	−10.06	±	0.24	−1.8
6	C109	Type 2	0.511742	±	0.000007	−17.33	±	0.13	0.282496	±	0.000025	−10.23	±	0.88	−1.9
8	C203	Type 3	0.511695	±	0.000015	−18.24	±	0.28	0.282640	±	0.000013	−5.14	±	0.44	3.9
11	C213-39	Type 3	0.511702	±	0.000008	−18.10	±	0.16	0.282592	±	0.000014	−6.84	±	0.48	2.0
12	C213-90	Type 3	0.511686	±	0.000009	−18.41	±	0.17	0.282623	±	0.000010	−5.73	±	0.36	3.4
13	C213-130	Type 3	0.511698	±	0.000006	−18.19	±	0.12	0.282619	±	0.000010	−5.86	±	0.37	3.1
14	C213-198	Type 1	0.511748	±	0.000011	−17.20	±	0.22	0.282505	±	0.000014	−9.91	±	0.49	−1.7

[a] 'Type 1': immature pellets containing Fe-bearing green clays. 'Type 2': moderately mature pellets dominated by Fe-bearing green clays. 'Type 3': mature pellets dominated by glauconite.

4. Results

4.1. Major and Trace Element Abundances

The measured major and trace concentrations in the acid leachate and clay-size fractions of the studied glauconitic grains are listed in Table S1. Potassium abundances ranged from K_2O ~0.6–4.7 wt% (mean: 2.6 ± 1.5 wt%; 1s.d.) and ~1.4–5.0 wt% (mean: 3.1 ± 1.4 wt%) in both the acid leachates and separated clays. These overall similar concentrations indicate that a substantial fraction of authigenic clay minerals was dissolved during 5 M HCl leaching. Iron also displayed similar abundances in both the acid leachates and clay-size fractions, with values ranging from ~14.8 to 39.2 wt% (mean: 26.1 ± 6.5 wt%) and ~13.0–36.3 wt% (mean: 24.8 ± 6.8 wt%), also suggesting that most HCl-extractable iron is derived from Fe-bearing authigenic clays. In contrast, while the Al contents varied significantly in the separated clays from Al_2O_3 ~4.5 to 19.4 wt%, the values observed in the acid leachates were relatively constant (~6.9 ± 1.8 wt%), suggesting limited kaolinite dissolution with 5 M HCl. As expected, Ca was more enriched in the acid leachates (CaO ~1.2–9.1 wt%) than in the separated clays (~0.01–0.06 wt%) due to the dissolution of biogenic material

and possibly calcium fluorapatite during HCl leaching. Rare earth element contents were significantly higher in the acid leachates than in the clay-size fractions, with Nd ranging from 15 to 50 ppm (mean: 35.2 ± 10.3 ppm) and 16 to 30 ppm (mean: 22.1 ± 5.0 ppm), respectively. In contrast, Hf abundances are higher in separated clays (mean: 2.4 ± 0.9 ppm) than in HCl leachates (mean: 0.9 ± 0.2 ppm).

4.2. Nd and Hf Isotope Compositions

The Nd and Hf isotopic ratios measured in this study are listed in Table 2. Both the acid leachates and clay-size fractions displayed overall similar Nd isotope compositions, yielding average ε_{Nd} values of −17.8 ± 0.7 (1 s.d.) and −17.7 ± 0.6, respectively (Figure 2b). These values are fully consistent with those previously reported for Congo glauconitic pellets [49]. In contrast, Hf isotope compositions were significantly more radiogenic in the acid leachates, ranging from ε_{Hf}~−4.9 to −0.9 (mean: −3.1 ± 1.0), relative to the separated clays (ε_{Hf}~−11.3 to −5.1; mean: −8.4 ± 2.4). Calculated $\Delta\varepsilon_{Hf\,CLAY}$ values, which correspond to the vertical ε_{Hf} deviation from the 'clay array', with an average of 5.5 ± 1.1 and 0.2 ± 2.9 in the acid leachates and clays, respectively (Figure 2b).

5. Discussion

5.1. Trace Element Behavior during Green Clay Authigenesis

Our major element data provide evidence that neoformed authigenic clays were near-quantitatively extracted during the 5 M HCl leaching step and that the Fe and K contents in both the acid leachable and clay-size fractions are thus largely controlled by the presence of Fe-bearing phyllosilicates formed following the alteration of detrital kaolinite. The process of green clay authigenesis at the Congo Shelf is illustrated when plotting the measured Fe_2O_3 and Al_2O_3 abundances versus the approximate age for the corresponding glauconite formation (Figure 4). This shows that the Fe and Al contents in authigenic clays increase and decrease, respectively, together with the estimated glauconite age and the degree of correlated authigenesis. Two ~20 kyr-old samples (C236; C213-198 cm) departed from the observed relationships (Figure 4), which could possibly reflect the sampling heterogeneity at the outer shelf, where surface sediment layers possibly contain glauconitic grains of various ages due to relatively low sedimentation rates. In contrast to Fe and Al, K abundances in both the acid leachates and separated clay fractions displayed no apparent correlation with either the water depth (plot not shown here) or approximate age of glauconite formation (Figure 4). This observation is in stark contrast to previous findings for the same area [41,42]. To some extent, this discrepancy could also be tentatively interpreted as reflecting sample heterogeneity. In particular, reworking of older glauconitic grains of the Miocene age from the outer edge region of the Congo Shelf could represent another explanation for this apparent discrepancy [48]. Fluctuations in the clay mineral composition of the sediment load exported by the Congo River could also possibly account for some of the observed discrepancy between the K content and the approximate age of the studied green pellets. The presence of up to ~25% of illite and chlorite in the marine muds deposited at the Congo Fan during the Late Quaternary [54] could have represented an additional source of K-bearing clay minerals in some of the studied peloid fractions. Additional elemental analyses of a larger suite of glauconitic grains would be required to further assess the degree to which the K contents co-vary with the glauconite formation age at the Congo Shelf. In any case, our dataset indicates that the Fe and Al contents for this particular suite of studied glauconitic pellets most likely represent more robust indicators than K for the degree of green clay authigenesis.

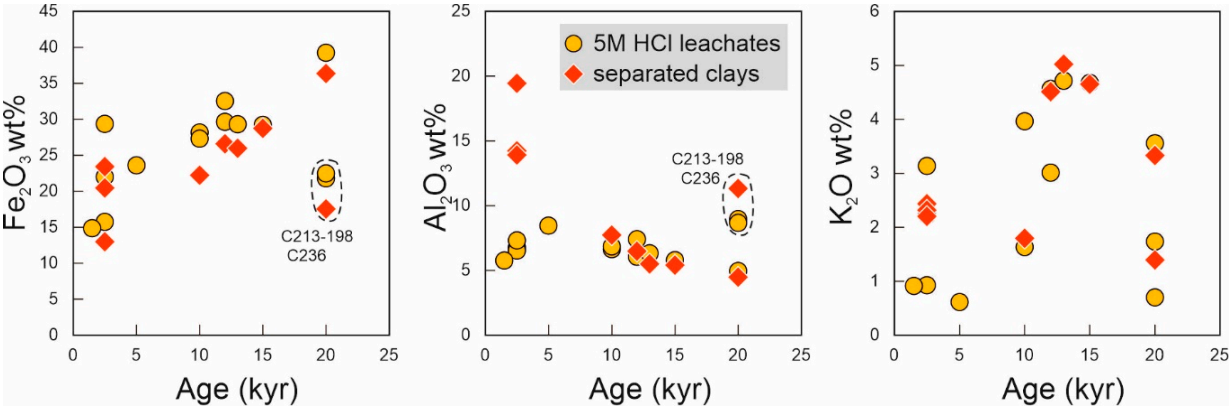

Figure 4. Relationships between the Fe_2O_3, Al_2O_3 and K_2O contents in Congo glauconitic pellets with the approximate age for the corresponding sediment [44,61]. Elemental data are presented for both the acid leachate and separated clay-size fractions of the studied green pellets. The Fe and Al contents in authigenic clays progressively increased and decreased, respectively, together with the estimated glauconite age and inferred degree of clay authigenesis. Two ~20 kyr-old samples (C236; C213-198) departed from the observed relationships, possibly reflecting sampling heterogeneity at the outer shelf.

The behavior of selected trace elements during clay authigenesis at the Congo Shelf can be assessed by normalizing concentrations for the separated clays to average values for Congo River-borne detrital clays. As an example, we considered here the clay-size fraction of C213-90 (~13 kyr B.P.), one of the 'Type 3′ samples characterized by the highest Fe_2O_3 (~25.9 wt%) and K_2O (~5.0 wt%) contents in this study (Figure 5). In Figure 5, the C213-90 data were also normalized for a comparison to the concentrations for the 'Type 1′ sample 70VB (~2–3 kyr B.P.), which presents evidence for limited authigenic clay formation (Fe_2O_3 ~13 wt%; K_2O ~2.2 wt%). As expected, the resulting diagrams clearly show that K, Fe, and Mg were significantly enriched during green clay authigenesis (up to ~300% relative to Congo River-borne detrital clays; Figure 5). Our data also indicated that significant gain occurred for Rb during glauconitization (~50%); an element that behaves similarly to K in Earth surface environments. In this study, the lower degree of Rb enrichment in authigenic clays compared to K (~6 times lower) confirms previous inferences that Rb is significantly less affected by post-depositional water–sediment exchange processes [62]. Furthermore, while the behavior of redox sensitive elements during glauconitization still remains poorly documented, our results suggest that green clay authigenesis can sequester substantial amounts of V, Mo, and Cr (up to ~85%), possibly reflecting the micro-reducing conditions associated with glauconite formation in fecal pellets [63]. Additionally, recent experimental work has demonstrated a strong binding mechanism for Cr when precipitating on clays through the substitution of Al [64], which could partly explain the observed Cr enrichment in authigenic Fe-bearing clays from the Congo Shelf. All other trace elements showed evidence for significant depletion in clays separated from glauconitic pellets compared to the initial kaolinite-rich material delivered by the Congo River, up to~−80% for Ba, Yb, Lu, Th, Ti, Y, and Sr (Figure 5). This observation provides support that kaolinite transformation and green clay authigenesis are accompanied by a net loss for many trace elements including REEs. Below, we discuss in detail the possible mechanisms accounting for the significant loss and decoupling of REEs during glauconitization and the associated isotopic shifts in neoformed authigenic clays. For other trace elements, future work will be required to further understand their behavior during green clay authigenesis.

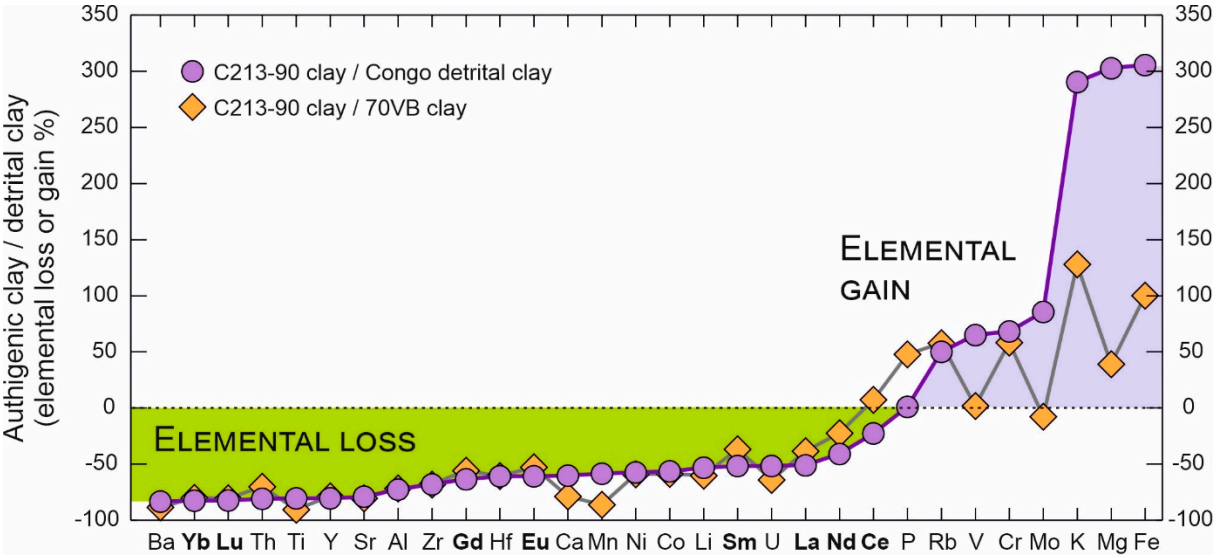

Figure 5. Behavior of selected trace elements during marine clay authigenesis at the Congo Shelf. Elemental concentrations for mature Fe-bearing authigenic clays (sample C213-90, with Fe_2O_3 ~25.9 wt% and K_2O ~5.0 wt%) normalized to both the average values for kaolinite-rich Congo River-borne detrital clays (purple circles; Table S1) and immature authigenic clays (orange diamonds; sample 70VB with K_2O ~2.2 wt% and the lowest Fe_2O_3 ~13 wt% content). The resulting diagrams indicate the elements that are gained (e.g., K, Fe, and Mg) or lost (expressed in %) during kaolinite dissolution and subsequent green clay authigenesis at the Congo Shelf. Rare earth elements are highlighted in bold.

5.2. Negligible Seawater Influence for Nd and Hf Isotopes in Marine Authigenic Clays

While a substantial fraction of HCl-extractable Fe is derived from authigenic clays (between ~80% and 93%, as inferred from the Fe_2O_3 content in both the acid leachates and separated clays), the observed relationship between Fe and ΣREE_N in acid leachates (i.e., the sum of shale-normalized REE abundances) suggests that the REE budget in bulk glauconite pellets (including both authigenic minerals and detrital clays) is also controlled by another Fe-rich phase (Figure 6). While displaying various shale-normalized REE patterns, HCl leachates of studied glauconitic pellets generally displayed a positive Ce-anomaly and mid-REE (MREE) enrichment relative to heavy-REE (Figure 7). This particular REE pattern is typical of Fe–Mn oxyhydroxide phases extracted from Congo Fan sediments, which mostly correspond to 'pre-formed' oxides associated with riverine inputs from the Congo River [65]. By analogy, we presume that the presence of such 'pre-formed' oxides could possibly influence the REE distribution in the authigenic, acid-extractable fraction of Congo glauconite pellets. An interesting feature in Figure 6 is the evidence that the 'Type 3′ samples exhibiting the highest ΣREE_N contents in acid leachates (e.g., C203, C213-90), which corresponded to mature green pellets, were also those that displayed the lowest ΣREE_N content in the associated clay-size fractions. This observation suggests that while ongoing glauconitization results in the progressive loss of REE in neoformed clay mineral phases (due to kaolinite dissolution; see discussion below), it also leads to significant REE enrichment in authigenic mineral phases such as presumably goethite and calcium fluorapatite precipitating from ambient bottom waters [49]. This latter hypothesis would be consistent with the fact that high ΣREE_N in acid leachates also coincide with relatively high P_2O_5 contents (Figure 6), hence further suggesting that authigenic (seawater-derived) phosphates could also play a role in controlling REE abundances in HCl leachates [49].

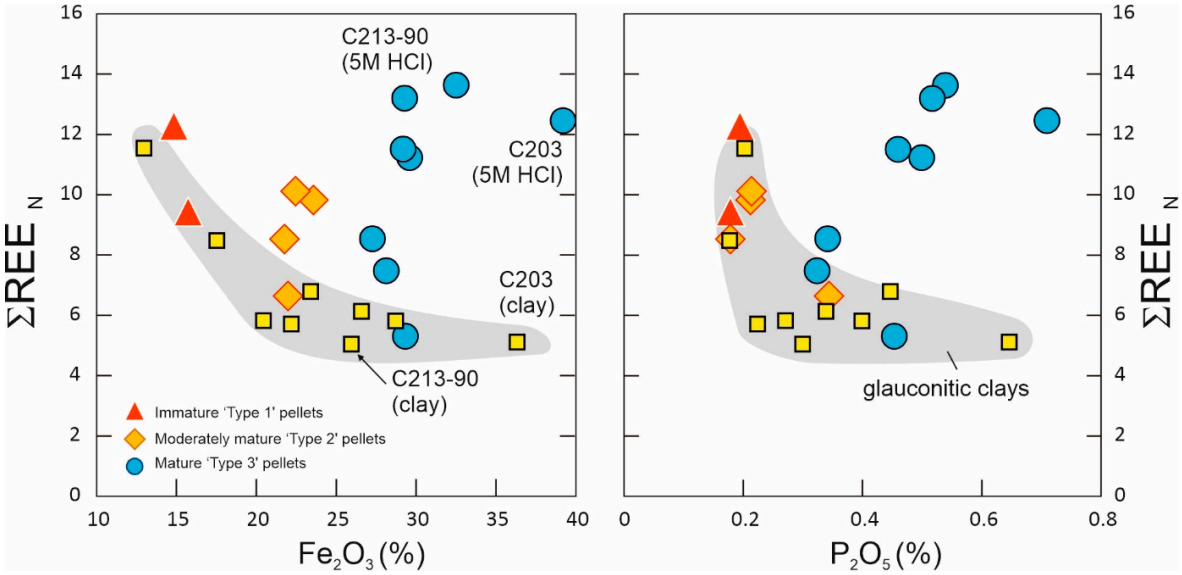

Figure 6. Relationships between the REE abundances and Fe_2O_3 and P_2O_5 contents in the acid leachates of Congo glauconite. ΣREE_N represents the sum of shale-normalized REE abundances (WRAS; [20]). Elemental data for the corresponding clay-size fractions (yellow boxes) are shown for comparison. 'Type 1′ samples correspond to immature multi-pellet samples containing Fe-bearing green clays, while 'Type 2′ samples are dominated by authigenic 7 Å Fe-rich mineral phases. 'Type 3′ samples correspond to mature glauconite-bearing samples. The observed relationships suggest that the REE budget in mature Fe-rich glauconite pellets (blue circles) is controlled by the presence of iron-rich mineral phases (e.g., neoformed goethite, Fe-oxyhydroxides associated with Congo terrigenous material) and authigenic, seawater-derived, calcium fluorapatite [49].

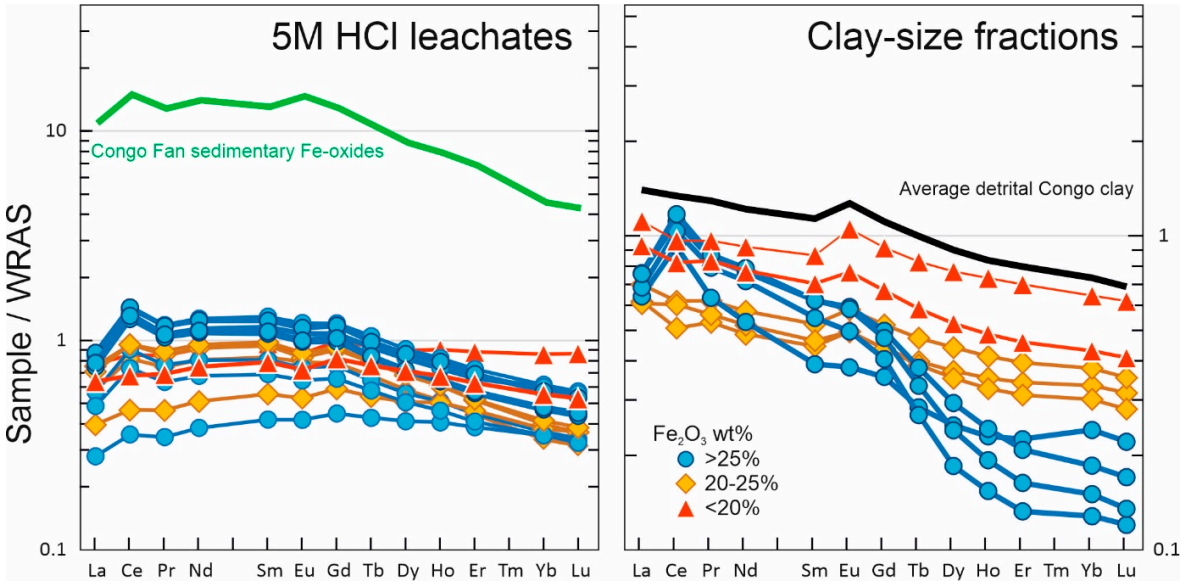

Figure 7. Shale-normalized (WRAS) REE patterns for the acid leachates and clay-size fractions of glauconite pellets from the Congo Shelf. Symbols correspond to the samples characterized by Fe_2O_3 <20% (red triangle; Type 1), 20%–25% (orange diamonds; Type 2), and >25% (blue circles; Type 3). Representative REE patterns for detrital clays (black line; Table S1) and Fe-oxyhydroxide phases [65] extracted from Congo Fan sediments are shown for comparison.

Unlike the acid leachates, the shale-normalized REE patterns of the separated clays displayed striking co-variation with the degree of glauconitization (Figure 7). The studied clay-size fractions showed a pronounced depletion in heavy rare earth elements (HREEs)

as the Fe content increased (Figure 7). These results confirm previous inferences that REE loss during glauconitization is accompanied by substantial REE decoupling [49,66]. Enhanced glauconite maturity and associated expulsion of detrital REE are thought to result in the progressive acquisition of seawater Nd isotope characteristics by the glauconitic pellets [49,66]. In this study, however, this hypothesis was not supported by the Nd isotope data for the clay-size fractions. While demonstrating a clear link with the degree of green clay authigenesis, as inferred from the observed correlation between ε_{Nd} and Fe_2O_3/Al_2O_3 (Figure 8), the Nd isotopes shifted toward more unradiogenic values (from ~−16.5 to −18.5) as the Fe content increased in the clay separates, hence markedly departing from the regional seawater ε_{Nd} values for upper surface waters in the study area (between ~−15.2 and −15.9 for the upper <300 m water column; [16]) (Figure 2b). The absence of any seawater REE signature in maturing authigenic clays is also supported by the Y/Ho ratio (i.e., a powerful proxy for tracing the relative contribution of seawater versus terrestrial signatures in marine sediments) [67]. In this study, all of the separated clay-size fractions displayed near-constant values (27.2 ± 1.0; Table S1), similar to that for Congo River detrital clays (26.9 ± 0.4; Table S1), hence further suggesting that neoformed clays do not integrate any substantial amount of REEs from ambient bottom waters. In contrast to clays, in the ε_{Nd} versus ε_{Hf} plot, many acid leachates fell between the fields defined by mature authigenic clays and the seawater end-member defined by the direct measurement of upper seawater waters in the study area [16] and sedimentary Fe-oxyhydroxides from the Congo Fan [32] (Figure 2b). This observation reinforces the view that while green clay authigenesis does not result in the acquisition of seawater isotope characteristics in neoformed clays, glauconite pellets formed at the Congo Shelf still include an authigenic 'seawater' component that can be extracted by HCl leaching, most likely corresponding to the presence of goethite, Fe-oxyhydroxide, and calcium fluorapatite phases [49].

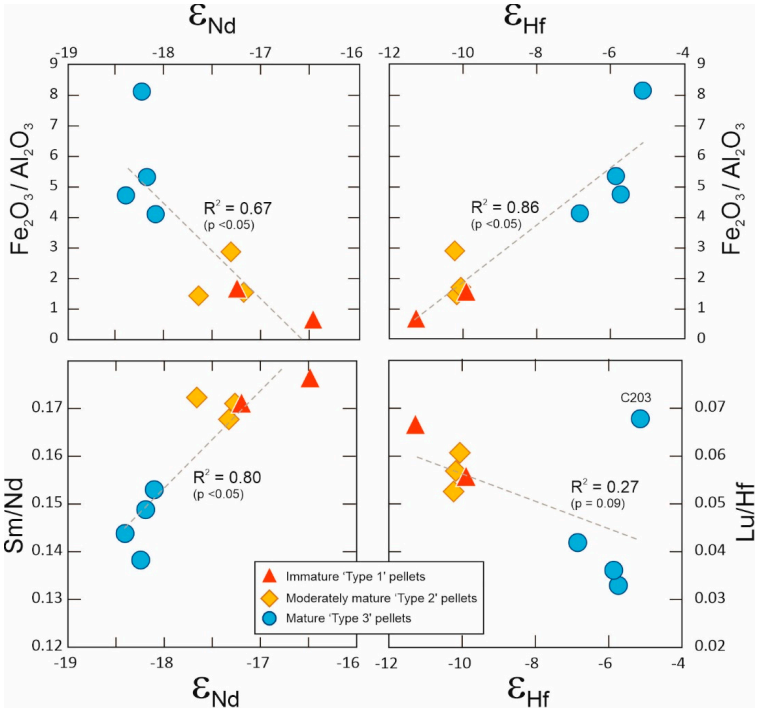

Figure 8. Relationships between the Nd and Hf isotope compositions, Fe_2O_3/Al_2O_3, and Sm/Nd and Lu/Hf elemental ratios in the clay-size fractions of the glauconite pellets. The measured ε_{Nd} and ε_{Hf} values co-varied with the degree of green clay authigenesis inferred from higher Fe/Al ratios. The observed relationships between the Nd–Hf radiogenic isotope ratios and parent–daughter elemental ratios reflect a mineralogical effect, corresponding to the progressive incorporation of a residual LREE-bearing accessory mineral phase characterized by low Sm/Nd and high Lu/Hf ratios.

5.3. Relict Accessory Phosphate Minerals Control REE Budget in Green Authigenic Clays

As discussed above, the observed Nd and Hf isotope shifts that accompany green clay authigenesis cannot be explained by any seawater influence. The measured ε_{Nd} and ε_{Hf} values also significantly departed from expected Congo River detrital source compositions. The Nd isotope composition of the suspended sediment load delivered by the Congo River is mostly governed by particulates from the Kasai left-bank tributary (ε_{Nd} -15.5 ± 0.7), with minor contributions from the Oubangui (-17.6 ± 0.4) and the Upper Congo/Lualaba (-17.6 ± 0.4) [47,68]. At present, modern sediments from the Congo Fan and the main Congo River tributaries plot near the clay array in the ε_{Nd} and ε_{Hf} diagram (Figure 2). Over the last 40 kyr B.P., the Congo terrigenous discharge has displayed relatively constant ε_{Nd} values fluctuating between -16.3 and -15.3 [46,47], while ε_{Hf} punctually departed from the clay array toward a less radiogenic composition (negative $\Delta\varepsilon_{Hf\,CLAY}$ values), particularly during periods of drier and cooler climate due to reduced chemical weathering conditions in the Congo Basin [46]. All of the above consideration indicates that the observed shifts toward unradiogenic ε_{Nd} and more radiogenic ε_{Hf} values in maturing authigenic clays at the Congo Shelf are unlikely to reflect a provenance change within the Congo Basin, nor any contribution from other regional sediment sources since the study area directly lies under the influence of the Congo River plume. Instead, we propose that the observed isotopic shifts during green clay authigenesis probably relates to a mineralogical effect, by which successive dissolution–crystallization events would result in the progressive concentration of a residual accessory mineral phase inert to alteration and characterized by low Sm/Nd and high Lu/Hf values. This hypothesis is supported by the evidence that the measured isotopic values in authigenic clays displayed strong correlations with both the Sm/Nd and Lu/Hf ratios (Figure 8). During the glauconitization process, whilst detrital REE become progressively depleted within neoformed clays (Figure 7), residual LREE-bearing accessory minerals characterized by low Sm/Nd and high Lu/Hf ratios could be incorporated within the clay mineral assemblages that constitute the green grains, thereby explaining the observed shifts toward more unradiogenic (low ε_{Nd}) and radiogenic (high ε_{Hf}) values, respectively.

To test this hypothesis, we investigated the mineralogical composition of a few green pellets from the 'Type 3′ sample C213-130 by SEM-EDS, which exhibited geochemical characteristics (e.g., Fe_2O_3 >25% and K_2O ~4.7%) of relatively 'mature' glauconitic grains on the Congo Shelf (Table 1). Our results provide direct evidence for the presence of micro-inclusions of heavy minerals in the glauconitic pellets (Figure 9). In fact, most of these micro-inclusions corresponded to small (<1 µm) LREE-bearing phosphate minerals with a chemical composition indicative of both LREE-rich aluminum-phosphate-sulfate (APS) minerals such as florencite (Figure 9C,D) and Th-rich LREE phosphate minerals such as monazite or rhabdophane (Figure 9G,H). While additional accessory mineral phases in the studied glauconitic pellets also include quartz, micro-inclusions of Ti-bearing minerals (ilmenite, rutile and/or anatase; Figure 9E) as well as very rare zircon grains, the ubiquitous presence of LREE-bearing phosphate phases in sample C213-130, with high contents of La, Ce, and Nd (several oxide weight percent for each element) provides strong evidence, despite their small size, that they are likely to strongly influence the REE budget of such mature glauconite pellets on the Congo Shelf.

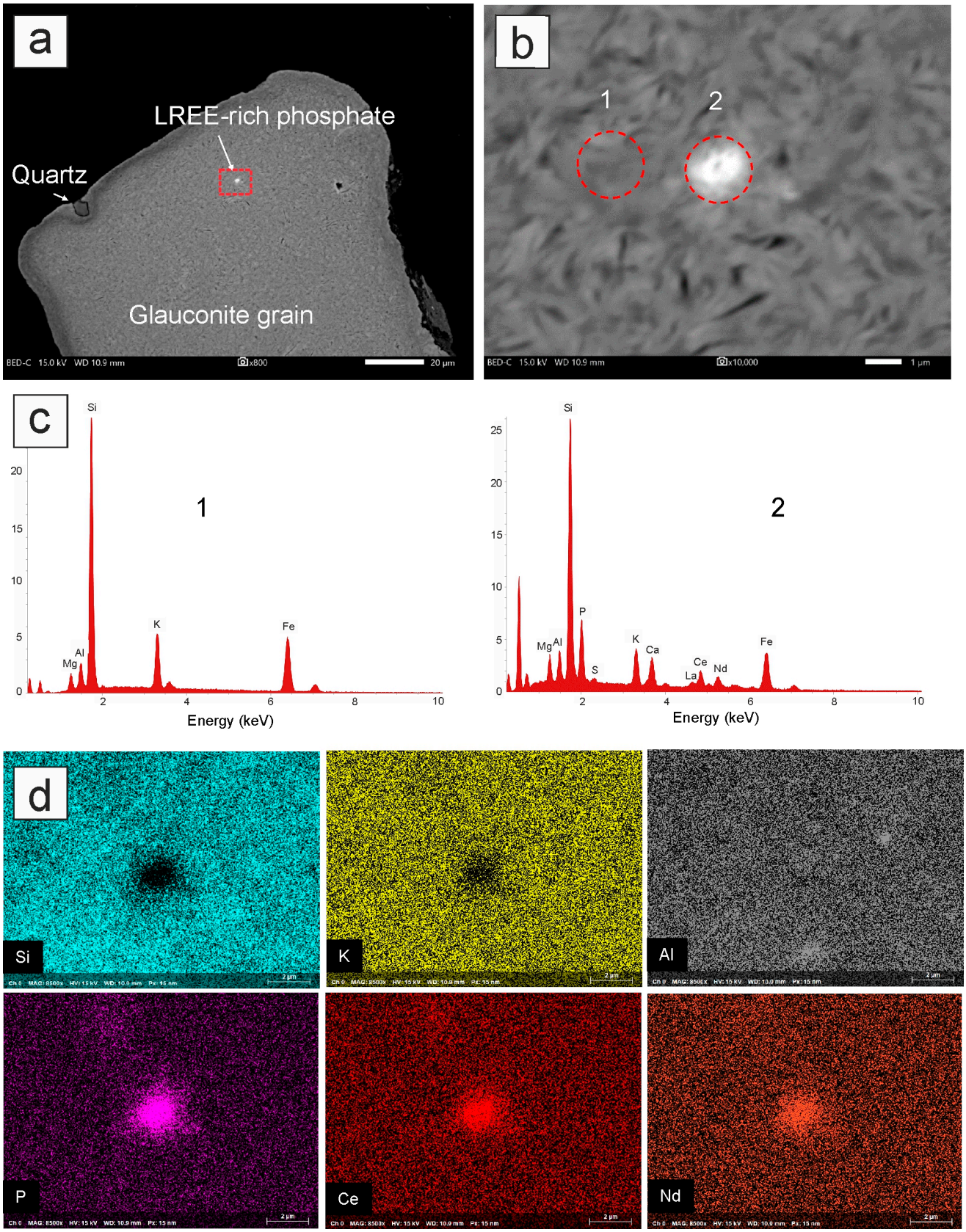

Figure 9. *Cont.*

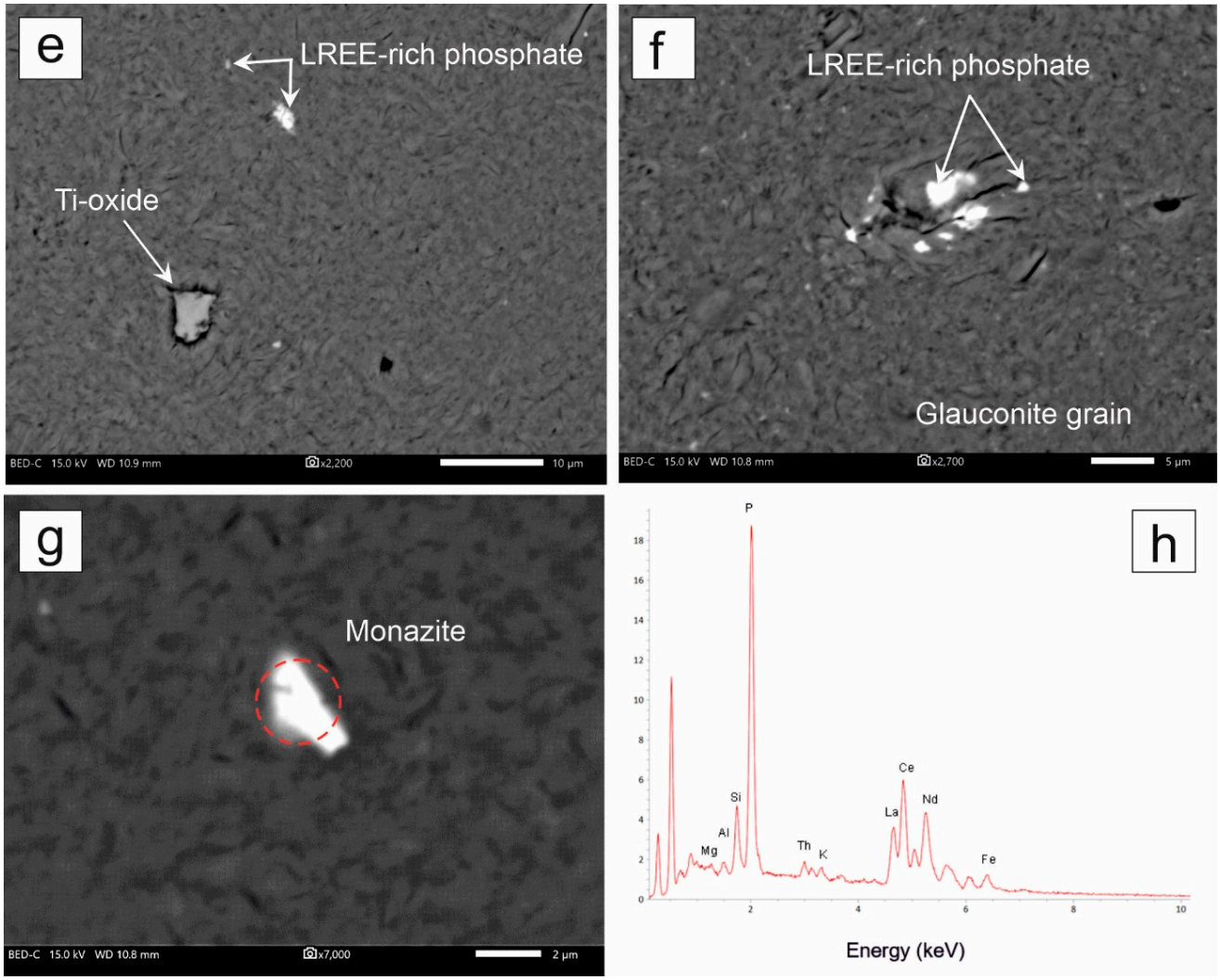

Figure 9. SEM-EDS observations and elemental mapping of Congo glauconitic pellets (sample C213). (**a**) SEM-BSE image showing the presence of a micro-inclusion of the LREE-bearing phosphate mineral. (**b**,**c**) The red circles correspond to two areas analyzed by EDS with the corresponding EDS spectrum indicating a micro-inclusion of LREE-rich phosphate embedded in Fe-bearing authigenic clays. Al, P, S, La, Ce, and Nd elements in the EDS spectrum of the micro-inclusion (2) are indicative of LREE-rich aluminum-phosphate-sulfate minerals (APS). (**d**) EDS mapping for a micro-inclusion of LREE-bearing APS. SEM-EDS observations and elemental mapping of Congo glauconitic pellets (sample C213). (**e**,**f**) SEM-BSE images showing evidence for multiple LREE-rich phosphate minerals and Ti-oxides in the glauconite grain. (**g**,**h**) SEM-BSE image and EDS spectrum of a LREE-rich monazite grain.

The proposed hypothesis is fully consistent with the evidence that in tropical regions, the chemical weathering of primary accessory minerals (e.g., apatite, allanite, monazite) in soil sequences releases substantial amounts of REE and phosphate, which typically result in the formation of secondary phosphate minerals intertwined in kaolinite in soil-saprolite profiles [69]. Secondary LREE-rich phosphate minerals such as APS minerals of the crandallite series rhabdophane have frequently been reported in tropical soils and laterites [70–73]. In tropical soils, the alteration of monazite can also result in the formation of Th-rich rhabdophane [74], hence suggesting that the Th-rich LREE-bearing phosphate mineral phases identified in sample C213-130 by SEM-EDS mapping (Figure 9G,H) could

possibly correspond to hydrated monazite formed by chemical weathering in the Congo Basin. These minerals typically occur as discrete <0.1–10 µm crystals, occurring in low abundance (>0.05 wt%) in most soils or sedimentary rocks and hence are difficult to identify using conventional microscopic techniques [75]. Importantly, these accessory minerals are stable up to 400–500 °C and remain insoluble over a wide range of pH and Eh conditions [76], meaning that they are unlikely to be affected by early marine diagenesis [75]. Recent micro-scale investigations have shown that these minerals dominate the LREE budget of kaolinite in tropical regions [77,78].

Based on the above consideration, we thus argue that as kaolinite dissolves during glauconitization, inherited nanocrystals of LREE-rich phosphate minerals become progressively incorporated into neoformed Fe-bearing clays. Such a mechanism would provide a plausible explanation accounting for both the pronounced LREE enrichment over HREE in authigenic clays. Because these minerals are directly derived from the alteration of primary phosphate minerals characterized by low Sm/Nd and high Lu/Hf ratios [21,26], their progressive incorporation into neoformed Fe-bearing clays on the Congo Shelf also clearly explains the observed shifts in Sm/Nd, Lu/Hf, ε_{Nd}, and ε_{Hf} during glauconitization. This observation is also fully consistent with the evidence that kaolinite-bearing river muds worldwide commonly display radiogenic Hf isotope compositions associated with positive $\Delta\varepsilon_{Hf\ clay}$ values (i.e., plotting 'above' the clay array; [35]).

5.4. Implications for the Impact of Clay Authigenesis on the Marine REE Cycling

To some extent, the proposed mechanism accounting for LREE enrichment in neoformed clays at the Congo Shelf compensates for the observed depletion in structural REEs caused by the dissolution of kaolinite silicate sheets. Indeed, despite the preservation of inherited REE-enriched accessory minerals in green authigenic clays, the formation of Fe-bearing clays is accompanied by a net loss of REEs (Figure 5). This loss can be quantified by normalizing the measured REE abundances to average values for detrital clays exported by the Congo River (Figure 10a), indicating that up to 80% of HREEs was lost during clay authigenesis. The resulting loss for LREE and, to a lesser extent, MREE, was less significant (between ~40% and 60%) due to the presence of accessory LREE-rich phosphate minerals. In comparison, only 10%–20% of Ce was lost during green clay authigenesis, which probably largely reflects the pronounced Ce enrichment observed in the micro-inclusions of LREE-bearing phosphate minerals (Figure 9). Alternatively, a greater stability of Ce^{4+} complexes during glauconitization relative to its neighboring REE^{3+} elements could also possibly account for the observed positive Ce anomaly in the clay-size fractions separated from mature glauconitic pellets.

Finally, our data can be used to determine the shale-normalized distribution pattern of the dissolved REE fraction released during kaolinite dissolution and subsequent clay authigenesis at the Congo margin (Figure 10b). Taking the example of the 'Type 3' samples C213-90 and C213-130, the resulting patterns displayed striking similarity with the average REE composition for seawater, characterized by positive La-anomaly, negative Ce-anomaly, and a gradual enrichment in HREEs (Figure 10b). While further investigation would be needed to assess whether similar findings can be obtained from the analysis of green pellets formed in other kaolinite-dominated shelf environments worldwide, these first results acquired on Congo glauconitic pellets provide direct support to previous inferences based on pore water analyses that clay mineral dissolution and the subsequent fractionation of REEs during uptake by authigenic clays could play a major role in the marine cycling of REEs (e.g., [13]).

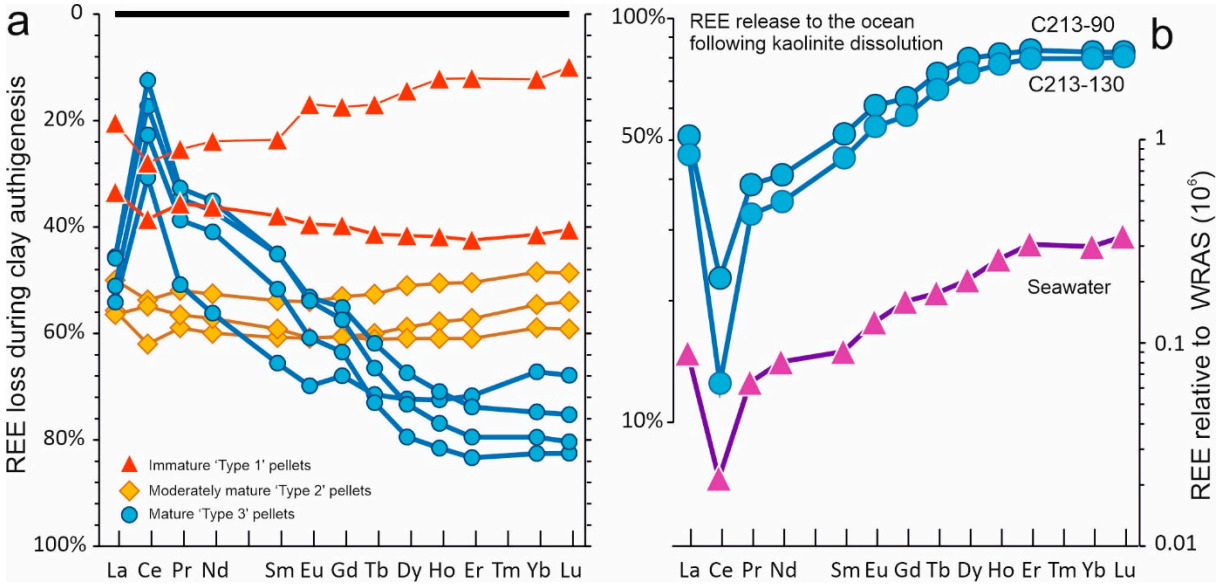

Figure 10. Impact of kaolinite dissolution and green clay authigenesis on the marine REE cycle. (**a**) Rare earth element abundances for the separated clay-size fractions of Congo glauconite normalized to the average kaolinite-rich detrital clay exported by the Congo River (thick black line; Table S1), expressed as loss %. (**b**) Shale-normalized distribution pattern of the dissolved REE fraction released during kaolinite dissolution and subsequent clay authigenesis at the Congo margin, taking the example of mature C213-90 and C213-130 glauconite samples. The average REE pattern for global seawater is also shown for comparison [79]. The observed similarity between the REE patterns for global seawater and the elemental fraction released from clay authigenesis suggests that reverse weathering processes at continental margins play a major role in the marine cycling of REEs.

6. Conclusions

Our geochemical investigation of glauconite grains from the Congo Shelf provides new evidence that reverse weathering processes at continental margins act as a net source of REEs to the ocean. At the Congo margin, kaolinite transformation into Fe-bearing clays is accompanied by significant REE depletion, up to 80% for the heavy-REEs. Neoformed clays display pronounced LREE enrichments, which we interpreted, using both Nd-Hf isotope measurements and SEM-EDS observations, as reflecting the entrapment of insoluble LREE-rich accessory mineral phases initially present within the kaolinite aggregates, presumably aluminum-phosphate-sulfate (APS) nanocrystals such as florencite and/or hydrated LREE phosphate (e.g., rhabdophane). Overall, our data indicate that the combination of kaolinite dissolution and subsequent entrapment of minor insoluble LREE-bearing mineral phases into aggregates of authigenic clays releases a dissolved REE fraction that strikingly displays seawater REE characteristics. This finding hence provides direct support that green clay authigenesis could play an important role in the marine REE cycle.

Supplementary Materials: The following supporting information can be downloaded at: https://www.mdpi.com/article/10.3390/min13081081/s1; Table S1: Major element and selected trace element compositions of acid-leachable (5M HCl) and clay-size (<2 μm) fractions of Congo shelf glauconies.

Author Contributions: Conceptualization, G.B. and P.G.; Methodology, G.B.; Formal analysis, G.B., M.-L.R. and B.G.; Investigation, G.B., P.G. and D.B.; Resources, P.G.; Writing—original draft preparation, G.B.; Writing—review and editing, P.G., H.C., M.-L.R., B.G., G.R.M., J.-A.B. and D.B.; Visualization, G.B.; Project administration, G.B.; Funding acquisition, G.B. All the authors contributed to data interpretation and writing the manuscript. All authors have read and agreed to the published version of the manuscript.

Funding: This work was funded by a grant to G.B. from the French National Research Agency (ANR-20-CE01-0003).

Data Availability Statement: The data presented in this study are openly available in Zenodo [https://doi.org/10.5281/zenodo.8087104].

Acknowledgments: We warmly thank N. Tanguy for providing the bathymetric map, M. Rovere for the sample preparation, and A. Trinquier for their assistance during the MC-ICPMS analyses. Two anonymous reviewers and D. Du are greatly acknowledged for providing insightful comments and for editorial handling, respectively.

Conflicts of Interest: The authors declare no conflict of interest.

References

1. Michalopoulos, P.; Aller, R.C. Rapid clay mineral formation in Amazon delta sediments: Reverse weathering and oceanic elemental cycles. *Science* **1995**, *270*, 614–617. [CrossRef]
2. Baldermann, A.; Warr, L.N.; Letofsky-Papst, I.; Mavromatis, V. Substantial iron sequestration during green-clay authigenesis in modern deep-sea sediments. *Nat. Geosci.* **2015**, *8*, 885–889.
3. Dunlea, A.G.; Murray, R.W.; Santiago Ramos, D.P.; Higgins, J.A. Cenozoic global cooling and increased seawater Mg/Ca via reduced reverse weathering. *Nat. Commun.* **2017**, *8*, 844. [CrossRef] [PubMed]
4. Ramos, D.P.S.; Morgan, L.E.; Lloyd, N.S.; Higgins, J.A. Reverse weathering in marine sediments and the geochemical cycle of potassium in seawater: Insights from the K isotopic composition ($^{41}K/^{39}K$) of deep-sea pore-fluids. *Geochim. Cosmochim. Acta* **2018**, *236*, 99–120. [CrossRef]
5. Baldermann, A.; Banerjee, S.; Czuppon, G.; Dietzel, M.; Farkaš, J.; Löhr, S.; Moser, U.; Scheiblhofer, E.; Wright, N.M.; Zack, T. Impact of green clay authigenesis on element sequestration in marine settings. *Nat. Commun.* **2022**, *13*, 1527.
6. Isson, T.T.; Planavsky, N.J. Reverse weathering as a long-term stabilizer of marine pH and planetary climate. *Nature* **2018**, *560*, 471–475. [CrossRef]
7. Trower, E.J.; Fischer, W.W. Precambrian Si isotope mass balance, weathering, and the significance of the authigenic clay silica sink. *Sedim. Geol.* **2019**, *384*, 1–11. [CrossRef]
8. Frank, M. Radiogenic isotopes: Tracers of past ocean circulation and erosional input. *Rev. Geophys.* **2002**, *40*, 1–38.
9. Goldstein, S.L.; Hemming, S.R. Long-lived isotopic tracers in oceanography, paleoceanography, and ice-sheet dynamics. In *Treatise on Geochemistry*; Elderfield, H., Turekian, K.K., Eds.; Elsevier: New York, NY, USA, 2003; Volume 6, pp. 453–489.
10. Bertram, C.J.; Elderfield, H. The geochemical balance of the rare earth elements and neodymium isotopes in the oceans. *Geochim. Cosmochim. Acta* **1993**, *57*, 1957–1986. [CrossRef]
11. Lacan, F.; Jeandel, C. Neodymium isotopes as a new tool for quantifying exchange fluxes at the continent–ocean interface. *Earth Planet. Sci. Lett.* **2005**, *232*, 245–257. [CrossRef]
12. Jeandel, C.; Oelkers, E.H. The influence of terrigenous particulate material dissolution on ocean chemistry and global element cycles. *Chem. Geol.* **2015**, *395*, 50–66.
13. Abbott, A.N.; Löhr, S.; Trethewy, M. Are clay minerals the primary control on the oceanic rare earth element budget? *Front. Mar. Sci.* **2019**, *6*, 504. [CrossRef]
14. Abbott, A.N.; Löhr, S.C.; Payne, A.; Kumar, H.; Du, J. Widespread lithogenic control of marine authigenic neodymium isotope records? Implications for paleoceanographic reconstructions. *Geochim. Cosmochim. Acta* **2022**, *319*, 318–336. [CrossRef]
15. Du, J.; Haley, B.A.; Mix, A.C.; Abbott, A.N.; McManus, J.; Vance, D. Reactive-transport modeling of neodymium and its radiogenic isotope in deep-sea sediments: The roles of authigenesis, marine silicate weathering and reverse weathering. *Earth Planet. Sci. Lett.* **2022**, *596*, 117792. [CrossRef]
16. Rahlf, P.; Laukert, G.; Hathorne, E.C.; Vieira, L.H.; Frank, M. Dissolved neodymium and hafnium isotopes and rare earth elements in the Congo River Plume: Tracing and quantifying continental inputs into the southeast Atlantic. *Geochim. Cosmochim. Acta* **2021**, *294*, 192–214. [CrossRef]
17. Hunt, H.R.; Summers, B.A.; Sieber, M.; Krisch, S.; Al-Hashem, A.; Hopwood, M.; Achterberg, E.E.; Conway, T.M. Distinguishing the influence of sediments, the Congo River, and water-mass mixing on the distribution of iron and its isotopes in the Southeast Atlantic Ocean. *Mar. Chem.* **2022**, *247*, 104181. [CrossRef]
18. Al-Hashem, A.A.; Beck, A.J.; Krisch, S.; Menzel Barraqueta, J.L.; Steffens, T.; Achterberg, E.P. Particulate trace metal sources, cycling, and distributions on the southwest African shelf. *Glob. Biogeochem. Cycles* **2022**, *36*, e2022GB007453. [CrossRef]
19. Goldstein, S.L.; O'nions, R.K.; Hamilton, P.J. A Sm-Nd isotopic study of atmospheric dusts and particulates from major river systems. *Earth Planet. Sci. Lett.* **1984**, *70*, 221–236. [CrossRef]
20. Bayon, G.; Toucanne, S.; Skonieczny, C.; André, L.; Bermell, S.; Cheron, S.; Dennielou, B.; Etoubleau, J.; Freslon, N.; Gauchery, T.; et al. Rare earth elements and neodymium isotopes in world river sediments revisited. *Geochim. Cosmochim. Acta* **2015**, *170*, 17–38. [CrossRef]
21. Bayon, G.; Vigier, N.; Burton, K.W.; Carignan, J.; Brenot, A.; Etoubleau, J.; Chu, N.C. The control of weathering processes on riverine and seawater hafnium isotope ratios. *Geology* **2006**, *34*, 433–436.

22. Rickli, J.; Frank, M.; Baker, A.R.; Aciego, S.; De Souza, G.; Georg, R.B.; Halliday, A.N. Hafnium and neodymium isotopes in surface waters of the eastern Atlantic Ocean: Implications for sources and inputs of trace metals to the ocean. *Geochim. Cosmochim. Acta* **2010**, *74*, 540–557. [CrossRef]
23. Rickli, J.; Frank, M.; Stichel, T.; Georg, R.B.; Vance, D.; Halliday, A.N. Controls on the incongruent release of hafnium during weathering of metamorphic and sedimentary catchments. *Geochim. Cosmochim. Acta* **2013**, *101*, 263–284. [CrossRef]
24. Patchett, P.J.; White, W.M.; Feldmann, H.; Kielinczuk, S.; Hofmann, A.W. Hafnium/rare earth element fractionation in the sedimentary system and crustal recycling into the Earth's mantle. *Earth Planet. Sci. Lett.* **1984**, *69*, 365–378.
25. Garçon, M.; Chauvel, C.; France-Lanord, C.; Huyghe, P.; Lavé, J. Continental sedimentary processes decouple Nd and Hf isotopes. *Geochim. Cosmochim. Acta* **2013**, *121*, 177–195. [CrossRef]
26. Dausmann, V.; Gutjahr, M.; Frank, M.; Kouzmanov, K.; Schaltegger, U. Experimental evidence for mineral-controlled release of radiogenic Nd, Hf and Pb isotopes from granitic rocks during progressive chemical weathering. *Chem. Geol.* **2019**, *507*, 64–84.
27. Rickli, J.; Frank, M.; Halliday, A.N. The hafnium–neodymium isotopic composition of Atlantic seawater. *Earth Planet. Sci. Lett.* **2009**, *280*, 118–127. [CrossRef]
28. Stichel, T.; Frank, M.; Rickli, J.; Hathorne, E.C.; Haley, B.A.; Jeandel, C.; Pradoux, C. Sources and input mechanisms of hafnium and neodymium in surface waters of the Atlantic sector of the Southern Ocean. *Geochim. Cosmochim. Acta* **2012**, *94*, 22–37. [CrossRef]
29. Albarede, F.; Simonetti, A.; Vervoort, J.D.; Blichert-Toft, J.; Abouchami, W. A Hf-Nd isotopic correlation in ferromanganese nodules. *Geophys. Res. Lett.* **1988**, *25*, 3895–3898. [CrossRef]
30. Vervoort, J.D.; Patchett, P.J.; Blichert-Toft, J.; Albarède, F. Relationships between Lu–Hf and Sm–Nd isotopic systems in the global sedimentary system. *Earth Planet. Sci. Lett.* **1999**, *168*, 79–99.
31. Vervoort, J.D.; Plank, T.; Prytulak, J. The Hf–Nd isotopic composition of marine sediments. *Geochim. Cosmochim. Acta* **2011**, *75*, 5903–5926. [CrossRef]
32. Bayon, G.; Burton, K.W.; Soulet, G.; Vigier, N.; Dennielou, B.; Etoubleau, J.; Ponzevera, E.; German, C.R.; Nesbitt, R.W. Hf and Nd isotopes in marine sediments: Constraints on global silicate weathering. *Earth Planet. Sci. Lett.* **2009**, *277*, 318–326. [CrossRef]
33. Garçon, M.; Chauvel, C.; France-Lanord, C.; Limonta, M.; Garzanti, E. Which minerals control the Nd–Hf–Sr–Pb isotopic compositions of river sediments? *Chem. Geol.* **2014**, *364*, 42–55. [CrossRef]
34. Zhao, W.; Sun, Y.; Balsam, W.; Lu, H.; Liu, L.; Chen, J.; Ji, J. Hf-Nd isotopic variability in mineral dust from Chinese and Mongolian deserts: Implications for sources and dispersal. *Sci. Rep.* **2014**, *4*, 5837.
35. Bayon, G.; Skonieczny, C.; Delvigne, C.; Toucanne, S.; Bermell, S.; Ponzevera, E.; André, L. Environmental Hf–Nd isotopic decoupling in World river clays. *Earth Planet. Sci. Lett.* **2016**, *438*, 25–36. [CrossRef]
36. Bayon, G.; Bindeman, I.N.; Trinquier, A.; Retallack, G.J.; Bekker, A. Long-term evolution of terrestrial weathering and its link to Earth's oxygenation. *Earth Planet. Sci. Lett.* **2022**, *584*, 117490.
37. Corentin, P.; Pucéat, E.; Pellenard, P.; Freslon, N.; Guiraud, M.; Blondet, J.; Adatte, T.; Bayon, G. Hafnium-neodymium isotope evidence for enhanced weathering and uplift-climate interactions during the Late Cretaceous. *Chem. Geol.* **2022**, *591*, 120724.
38. Chen, H.; Bayon, G.; Xu, Z.; Li, T. Hafnium isotope evidence for enhanced weatherability at high southern latitudes during Oceanic Anoxic Event 2. *Earth Planet. Sci. Lett.* **2023**, *601*, 117910. [CrossRef]
39. Babonneau, N.; Savoye, B.; Cremer, M.; Klein, B. Morphology and architecture of the present canyon and channel system of the Zaire deep-sea fan. *Mar. Petrol. Geol.* **2022**, *19*, 445–467. [CrossRef]
40. Giresse, P. Quaternary Glauconitization on Gulf of Guinea, Glauconite Factory: Overview of and New Data on Tropical Atlantic Continental Shelves and Deep Slopes. *Minerals* **2022**, *12*, 908. [CrossRef]
41. Giresse, P.; Wiewiora, A.; Lacka Lącka, B. Mineral phases and processes within green peloids from two recent deposits near the Congo River mouth. *Clays Clay Miner.* **1988**, *23*, 447–458.
42. Odin, G.S. Glaucony from the Gulf of Guinea. In *Green Marine Clays. Oolitic Ironstones, Verdine Facies, Glaucony Facies and Celadonite-Bearing Facies—A Comparative Study*; Odin, G.S., Ed.; Elsevier: Amsterdam, The Netherlands, 1988; Volume 45, pp. 225–247.
43. Amouric, M.; Parron, C.; Casalini, L.; Giresse, P. A (1: 1) 7-Å Fe phase and its transformation in recent sediments: An HRTEM and AEM study. *Clays Clay Miner.* **1995**, *43*, 446–454. [CrossRef]
44. Giresse, P. Essai de chronomètrie de la glauconitisation dans le Golfe de Guinée; exemple de vitesse diagénétique au Quaternaire supèrieur. *CR Somm. Soc. Geol. Fr.* **1975**, *4*, 163–164.
45. Wiewióra, A.; Lacka, B.; Giresse, P. Characterization and origin of 1: 1 phyllosilicates within peloids of the Recent, Holocene and Miocene deposits of the Congo Basin. *Clay Clay Min.* **1996**, *44*, 587–598. [CrossRef]
46. Bayon, G.; Dennielou, B.; Etoubleau, J.; Ponzevera, E.; Toucanne, S.; Bermell, S. Intensifying weathering and land use in Iron Age Central Africa. *Science* **2012**, *335*, 1219–1222. [CrossRef] [PubMed]
47. Bayon, G.; Schefuß, E.; Dupont, L.; Borges, A.V.; Dennielou, B.; Lambert, T.; Mollenhauer, G.; Monin, L.; Ponzevera, E.; Skonieczny, C.; et al. The roles of climate and human land-use in the late Holocene rainforest crisis of Central Africa. *Earth Planet. Sci. Lett.* **2019**, *505*, 30–41. [CrossRef]
48. Wiewióra, A.; Giresse, P.; Jaunet, A.M.; Wilamowski, A.; Elsass, F. Crystal chemistry of layer silicates of the Miocene green grain (Congo Basin) from Transmission Electron Microscopy (TEM) and Analytical Electron Microscopy (AEM) observations. *Clays Clay Min.* **1999**, *47*, 582–590.

49. Stille, P.; Clauer, N. The process of glauconitization: Chemical and isotopic evidence. *Contrib. Min. Petrol.* **1994**, *117*, 253–262. [CrossRef]
50. Giresse, P.; Jansen, J.H.F.; Kouyoumontzakis, G.; Moguedet, G. Les fonds de la plateforme congolaise, le delta sous-marin du fleuve Congo. Bilan de huit ans de recherches sédimentologiques, pal6ontologiques, géochimiques et géophysiques. *Trav. Doc. ORSTOM* **1981**, *138*, 13–45.
51. Giresse, P. Le fer et les glauconies au large du fleuve Congo. *Sci. Geol. Bull. Mem.* **1985**, *38*, 293–322. [CrossRef]
52. Giresse, P.; Aloïsi, J.C.; Kuete, M.; Monteillet, J.; Ngueutchoua, G. Quaternary sedimentary deposits on the Cameroon shelf: Characterization of facies and late Quaternary shorelines. *Quat. Int.* **1995**, *29*, 75–87. [CrossRef]
53. Giresse, P.; Odin, G.S. Nature minéralogique et origine des glauconies du plateau continental du Gabon et du Congo. *Sedimentology* **1973**, *20*, 457–488. [CrossRef]
54. Gingele, F.X.; Müller, P.M.; Schneider, R.R. Orbital forcing of freshwater input in the Zaire Fan area—Clay mineral evidence from the last 200 kyr. *Palaeogeog. Palaeoclimatol. Palaeoecol.* **1998**, *138*, 17–26. [CrossRef]
55. Barrat, J.A.; Keller, F.; Amossé, J.; Taylor, R.N.; Nesbitt, R.W.; Hirata, T. Determination of rare earth elements in sixteen silicate reference samples by ICP-MS after Tm addition and ion exchange separation. *Geostand. Newslett.* **1996**, *20*, 133–139. [CrossRef]
56. Barrat, J.A.; Zanda, B.; Moynier, F.; Bollinger, C.; Liorzou, C.; Bayon, G. Geochemistry of CI chondrites: Major and trace elements, and Cu and Zn isotopes. *Geochim. Cosmochim. Acta* **2012**, *83*, 79–92. [CrossRef]
57. Chu, N.C.; Taylor, R.N.; Chavagnac, V.; Nesbitt, R.W.; Boella, R.M.; Milton, J.A.; German, C.R.; Bayon, G.; Burton, K. Hf isotope ratio analysis using multi-collector inductively coupled plasma mass spectrometry: An evaluation of isobaric interference corrections. *J. Anal. Atom. Spectrom.* **2002**, *17*, 1567–1574. [CrossRef]
58. Tanaka, T.; Togashi, S.; Kamioka, H.; Amakawa, H.; Kagami, H.; Hamamoto, T.; Yuhara, M.; Orihashi, Y.; Yoneda, S.; Shimizu, H.; et al. JNdi-1: A neodymium isotopic reference in consistency with LaJolla neodymium. *Chem. Geol.* **2000**, *168*, 279–281. [CrossRef]
59. Blichert-Toft, J.; Chauvel, C.; Albarède, F. Separation of Hf and Lu for high-precision isotope analysis of rock samples by magnetic sector-multiple collector ICP-MS. *Contrib. Min. Petrol.* **1997**, *127*, 248–260. [CrossRef]
60. Bouvier, A.; Vervoort, J.D.; Patchett, P.J. The Lu–Hf and Sm–Nd isotopic composition of CHUR: Constraints from unequilibrated chondrites and implications for the bulk composition of terrestrial planets. *Earth Planet. Sci. Lett.* **2008**, *273*, 48–57. [CrossRef]
61. Giresse, P. Réponse aux observations de G.S. Odin relative à la note sur «Essai de chronométrie de la glauconitisation dans le golfe de Guinée . . .» Compléments et remarques. *CR Somm. Soc. Geol. Fr.* **1976**, *3*, 108–111.
62. van de Kamp, P.C. Potassium distribution and metasomatism in pelites and schists: How and when, relation to postdepositional events. *J. Sedim. Res.* **2016**, *86*, 683–711. [CrossRef]
63. Tribovillard, N.; Bout-Roumazeilles, V.; Abraham, R.; Ventalon, S.; Delattre, M.; Baudin, F. The contrasting origins of glauconite in the shallow marine environment highlight this mineral as a marker of paleoenvironmental conditions. *Comptes Rendus Géoscience* **2023**, *355*, 1–16. [CrossRef]
64. Hao, W.; Chen, N.; Sun, W.; Mänd, K.; Kirsimäe, K.; Teitler, Y.; Somelar, P.; Robbins, L.J.; Babechuck, M.G.; Planavsky, N.J.; et al. Binding and transport of Cr (III) by clay minerals during the Great Oxidation *Earth Planet. Sci. Lett.* **2022**, *584*, 117503.
65. Bayon, G.; German, C.R.; Burton, K.W.; Nesbitt, R.W.; Rogers, N. Sedimentary Fe–Mn oxyhydroxides as paleoceanographic archives and the role of aeolian flux in regulating oceanic dissolved REE. *Earth Planet. Sci. Lett.* **2004**, *224*, 477–492. [CrossRef]
66. Giresse, P.; Bayon, G.; Tallobre, C.; Loncke, L. Neodymium Isotopes in Glauconite for Palaeoceanographic Reconstructions at Continental Margins: A Preliminary Investigation From Demerara Rise. *Front. Earth Sci.* **2021**, *9*, 652501. [CrossRef]
67. Nozaki, Y.; Zhang, J.; Amakawa, H. The fractionation between Y and Ho in the marine environment. *Earth Planet. Sci. Lett.* **1997**, *148*, 329–340.
68. Allègre, C.J.; Dupré, B.; Négrel, P.; Gaillardet, J. Sr-Nd-Pb isotope systematics in Amazon and Congo River systems: Constraints about erosion processes. *Chem. Geol.* **1996**, *131*, 93–112. [CrossRef]
69. Banfield, J.F.; Eggleton, R.A. Apatite replacement and rare earth mobilization, fractionation, and fixation during weathering. *Clays Clay Miner.* **1989**, *37*, 113–127.
70. Braun, J.J.; Pagel, M.; Muller, J.P.; Bilong, P.; Michard, A.; Guillet, B. Cerium anomalies in lateritic profiles. *Geochim. Cosmochim. Acta* **1990**, *54*, 781–795.
71. Seghal, J. *Red and Lateritic Soils*; Balkema: Rotterdam, The Netherlands, 1998; 453p.
72. Dill, H.G. The geology of aluminium phosphates and sulphates of the alunite group minerals: A review. *Earth Sci. Rev.* **2001**, *53*, 35–93. [CrossRef]
73. Lima da Costa, M.; Sabá Leite, A.; Pöllmann, H. A laterite-hosted APS deposit in the Amazon region, Brasil: The physical-chemical regime and environment of formation. *J. Geochem. Explor.* **2016**, *170*, 107–124.
74. Berger, A.; Gnos, E.; Janots, E.; Fernandez, A.; Giese, J. Formation and composition of rhabdophane, bastnäsite and hydrated thorium minerals during alteration: Implications for geochronology and low-temperature processes. *Chem. Geol.* **2008**, *254*, 238–248.
75. Rasmussen, B. Early-diagenetic REE-phosphate minerals (florencite, gorceixite, crandallite, and xenotime) in marine sandstones; a major sink for oceanic phosphorus. *Am. J. Sci.* **1996**, *296*, 601–632. [CrossRef]
76. Kohlitsch, U.; Pring, A. Crystal-chemistry of the crandallite, beudantite and the alunite groups: A review and evaluation of the suitability as storage material for toxic metals. *J. Mineralog. Petrol. Sci.* **2001**, *96*, 67–78.

77. Ji, B.; Zhang, W. The effect of mechanical grinding and thermal treatment on the recovery of rare earth elements (REEs) from kaolinite. *Powder Technol.* **2021**, *394*, 622–631.
78. Gaudin, A.; Ansan, V.; Lorand, J.P.; Pont, S. Genesis of a florencite-bearing kaolin deposit on ordovician schists at Saint-Aubin-des-Châteaux, Armorican Massif, France. *Ore Geol. Rev.* **2020**, *120*, 103445.
79. Bayon, G.; Lemaitre, N.; Barrat, J.A.; Wang, X.; Feng, D.; Duperron, S. Microbial utilization of rare earth elements at cold seeps related to aerobic methane oxidation. *Chem. Geol.* **2020**, *555*, 119832.

Disclaimer/Publisher's Note: The statements, opinions and data contained in all publications are solely those of the individual author(s) and contributor(s) and not of MDPI and/or the editor(s). MDPI and/or the editor(s) disclaim responsibility for any injury to people or property resulting from any ideas, methods, instructions or products referred to in the content.